17th International Symposium on Ice
Saint Petersburg, Russia, 21-25 June 2004
International Association of Hydraulic Engineering and Research

ON PREDICTABILITY OF ELASTIC-PLASTIC SEA ICE DYNAMICS MODELS

Robert S. Pritchard[1]

ABSTRACT

Certain viscous-plastic (VP) models are unstable during all opening deformations and some closing deformations. Thus, their behavior is chaotic. Attention now turns to stability of elastic-plastic (EP) models, which are used less frequently, but are useful alternatives to VP models, especially for shorter-term simulations. The EP model is studied when behavior is elastic and when stress is on the tensile cutoff cone during opening deformations. To analyze stability, we introduce perturbations to solutions, linearize the perturbation equations, introduce modal solutions to the linear perturbation equations, and look for modes that grow. Modes that can grow are sensitive to initial conditions and are therefore chaotic. This analysis shows that the EP model is stable when stress is within or on the tensile cutoff cone.

INTRODUCTION

This study has the goal of determining whether or not an EP sea ice dynamics model is stable. The central idea is to determine if ice dynamics models have solutions that are sensitive to initial conditions. If solutions are sensitive to initial conditions, then small perturbations to the initial conditions grow, making solutions unpredictable and inaccurate. Such behavior is chaotic. Unstable models might have acceptable behavior for some time interval, but solutions that are similar initially will eventually diverge, which implies that unstable models will eventually lose predictability. Although a user might choose to use a chaotic model, such models require a statistical presentation of results, and we believe it is better to use a stable model. At a minimum, it is essential to know if behavior is chaotic.

BACKGROUND

Gray and Killworth (1995) and *Gray* (1999) showed that the *Hibler* (1979) VP model is unstable during uniaxial opening when the ice condition is described by the standard two-component approximation to the thickness distribution. *Pritchard* (2002) presented a method for analyzing model stability during general deformation states. Linearized

[1] IceCasting, Inc., 20 Wilson Court, San Rafael, CA 94901-1230, USA.; http://www.icecasting.com.

perturbation equations were introduced for generic EP and VP models. The linear perturbation equations were solved by introducing modes, and the growth or decay of each mode was determined. We take this perturbation approach here, assuming that a model is stable and problems are well posed if small perturbations to the initial conditions give rise to small perturbations to the solution, and that these perturbations decay with time (*Schreyer*, 2001).

In *Pritchard* (2003), a quasi-steady form of the *Hibler* (1979) VP model was analyzed. By discarding the inertia, the momentum and VP law perturbation equations were reduced to algebraic constraints. Evolution of ice conditions and strength provided time dependent behavior, and one eigenvalue for each mode. During all opening deformations and during some closing deformations, the modes were found to grow. Thus, the quasi-steady VP model is not stable. More recently, *Pritchard* (2004) has showed that the fully dynamic VP model is also unstable in all opening deformations and some closing deformations. These were essential first steps toward understanding the chaotic behavior of the popular VP model.

ELASTIC-PLASTIC MODEL

The elements of an ice dynamics model are momentum balance equation, constitutive law relating stress and deformation, ice conditions evolution equations, and hardening law. The model discussed here represents only part of the complete EP model, namely, when stress is inside the yield surface or on the tensile cutoff cone. Thus, we do not discuss the ice condition evolution equations or the hardening law.

Momentum Balance

The momentum equation balances inertial, Coriolis, and tilt accelerations against the applied air and water stresses and divergence of the internal stress

$$m\frac{d\mathbf{v}}{dt} + \mathbf{b} = \boldsymbol{\tau} + \nabla \cdot \boldsymbol{\sigma} . \tag{1}$$

The body force **b**(**v**) contains the Coriolis and water drag forces that depend on ice velocity **v**, and $\boldsymbol{\tau}$ contains air drag and sea surface tilt forces that are independent of ice velocity, m is mass per unit area and $\boldsymbol{\sigma}$ is internal ice stress resultant in excess of hydrostatic equilibrium (stress for short). The equations are expressed in a Lagrangian description where t is time, d/dt is material rate, x is spatial position, and ∇ is spatial gradient.

Elastic-Plastic Constitutive Law

Coon et al. (1974) introduced an isotropic elastic-plastic constitutive law that describes the large deformations observed in sea ice motions. The plasticity law assumes that the stress state cannot violate the isotropic yield criterion

$$\phi\left(\sigma_I, \sigma_{II}, p^*\right) \le 0 , \tag{2}$$

where $\boldsymbol{\sigma}$ is stress and p^* is isotropic compressive strength. The isotropic yield surface depends on the average normal stress $\sigma_I = \frac{1}{2}\boldsymbol{\sigma} : \mathbf{1}$ and the shear stress invariant $\sigma_{II} = \sqrt{\frac{1}{2}\boldsymbol{\sigma}' : \boldsymbol{\sigma}'}$, where the stress deviator is $\boldsymbol{\sigma}' = \boldsymbol{\sigma} - \sigma_I \mathbf{1}$. Operator**:** is the double inner product of the two second-order tensors.

Pritchard (1975, 1981) chose the diamond yield surface shown in Figure 1. One reason was that stress states on the tensile cutoff cone would be stable in the sense of *Drucker* (1959). A second reason was that the nonzero unconfined compressive strength would simulate arching observed across the Bering Strait (e.g., *Pritchard, Reimer, and Coon*, 1979). *Pritchard* (1998) showed that all isotropic yield surfaces resulting from an anisotropic law must lie within or on the diamond yield surface.

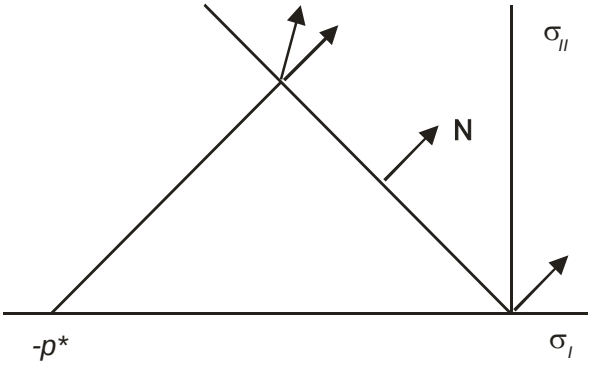

Fig. 1. Diamond yield surface shown in stress invariant space

An associated flow rule is assumed so that plastic stretching $\mathbf{D}_p$ is normal to the isotropic yield surface

$$\mathbf{D}_p = \frac{\lambda}{2}\left(\frac{\partial \phi}{\partial \sigma_I}\mathbf{1} + \frac{\partial \phi}{\partial \sigma_{II}}\frac{\boldsymbol{\sigma}'}{\sigma_{II}}\right), \tag{3}$$

where λ is a non-negative scalar variable. In the figure, we use $\mathbf{N} = \partial\phi/\partial\boldsymbol{\sigma}$ to indicate the normal tensor. When stress is at a corner of the yield surface, the plastic stretching must be within the fan defined by the normal tensors to each of the surfaces through that stress state.

For an elastic-plastic material, the stress satisfies a linear elastic law

$$\dot{\boldsymbol{\sigma}} = \mathbf{M} : \dot{\mathbf{e}} \ , \tag{4}$$

where **M** is the elastic modulus tensor, **e** is the elastic strain. The overhead dot represents a material rate and here the operator **:** is the double inner product of the fourth and second-order tensors. The isotropic form of the elastic response is

$$\dot{\boldsymbol{\sigma}} = \left(M_I - M_{II}\right)\dot{e}_I \mathbf{1} + 2M_{II}\dot{\mathbf{e}}, \tag{5}$$

where M_I and M_{II} are the bulk and shear moduli, respectively, and $e_I = \mathbf{e} : \mathbf{1}$.

The elastic strain rate and plastic stretching are related kinematically by (*Pritchard*, 1975)

$$\dot{\mathbf{e}} - \mathbf{W}\cdot\mathbf{e} + \mathbf{e}\cdot\mathbf{W} = \mathbf{D} - \mathbf{D}_p \ , \tag{6}$$

where **D** is stretching and **W** is spin, which are the symmetric and anti-symmetric parts of the velocity gradient **L**, respectively. These kinematic variables provide a frame-invariant description that accounts for spin of the stress tensor at the rate of rigid body rotation. Here we neglect rigid body rotation, and consider only non-rotating solutions.

The equations can be combined (e.g., *Pritchard*, 2002) into a single rate type equation

$$\dot{\boldsymbol{\sigma}} = \mathbf{M}_{ep} : \mathbf{D} + \mathbf{M}_{p^*} \dot{p}^*, \tag{7}$$

where the EP modulus $\mathbf{M}_{ep}$ is a fourth-order tensor and the strength modulus $\mathbf{M}_{p^*}$ is a second-order tensor. They are given by

$$\mathbf{M}_{ep} = \mathbf{M} - \frac{\left(\mathbf{M} : \dfrac{\partial \phi}{\partial \boldsymbol{\sigma}}\right) \otimes \left(\dfrac{\partial \phi}{\partial \boldsymbol{\sigma}} : \mathbf{M}\right)}{\dfrac{\partial \phi}{\partial \boldsymbol{\sigma}} : \mathbf{M} : \dfrac{\partial \phi}{\partial \boldsymbol{\sigma}}} \quad , \qquad \mathbf{M}_{p^*} = -\frac{\left(\mathbf{M} : \dfrac{\partial \phi}{\partial \boldsymbol{\sigma}}\right) \dfrac{\partial \phi}{\partial p^*}}{\dfrac{\partial \phi}{\partial \boldsymbol{\sigma}} : \mathbf{M} : \dfrac{\partial \phi}{\partial \boldsymbol{\sigma}}}. \tag{8}$$

Operator $\otimes$ is the outer product of tensors, which are both second order tensors.

Three special cases are analyzed. First, stress is within the yield surface. The EP modulus is the elastic modulus $\mathbf{M}_{ep} = \mathbf{M}$ and the strength modulus is zero $\mathbf{M}_{p^*} = \mathbf{0}$. Second, stress is on the tensile cutoff cone. The strength modulus tensor is zero $\mathbf{M}_{p^*} = \mathbf{0}$. Third, stress is at the origin $\boldsymbol{\sigma} = \mathbf{0}$. The modulus tensors are zero $\mathbf{M}_{ep} = \mathbf{0}$ and $\mathbf{M}_{p^*} = \mathbf{0}$.

STABILITY ANALYSIS

Each primary solution variable is perturbed, and the equations governing the perturbations are derived. The perturbation equations are linearized about the solution. These linear equations are solved by the usual modal analysis. To do so, we consider locally uniform solutions so that the partial differential equations have constant coefficients. The modal solutions are spatial trigonometric functions (an infinite set of complex exponentials $e^{ik\mathbf{n}\cdot\mathbf{x}/L}$). Thus, the velocity and stress perturbations are assumed in the form

$$\hat{\mathbf{v}} = \overline{\mathbf{v}}(t) e^{\frac{ik}{L}\mathbf{v}\mathbf{n}\cdot\mathbf{x}}, \qquad \hat{\boldsymbol{\sigma}} = \overline{\boldsymbol{\sigma}}(t) e^{\frac{ik}{L}\mathbf{n}\cdot\mathbf{x}}, \tag{9}$$

where k is an integer index, $\mathbf{n}$ is an arbitrary unit length direction vector, and L is a length scale. Each spatial eigenvector is multiplied by a time-dependent coefficient that is determined as the solution of a system of ordinary differential equations. We analyze this set of ordinary differential equations to learn if modes grow or decay when external forcing is zero.

Momentum Balance Perturbation Equation

The momentum balance perturbation equation satisfies (*Pritchard*, 2002, 2004)

$$m \frac{d\hat{\mathbf{v}}}{dt} + \mathbf{b}' \cdot \hat{\mathbf{v}} = \hat{\boldsymbol{\tau}} + \nabla \cdot \hat{\boldsymbol{\sigma}}, \tag{10}$$

where water stress is a quadratic function of ice velocity and

$$\mathbf{b}' = mf\, \mathbf{B}_{\pi/2} + \rho_w C_w \mathbf{B}_w \cdot \left(\frac{\mathbf{v} \otimes \mathbf{v}}{|\mathbf{v}|} + |\mathbf{v}|\mathbf{1} \right). \tag{11}$$

The operator $\mathbf{B}_{\pi/2}$ describes rotation counterclockwise through ninety degrees and $\mathbf{B}_w$ through angle β. Water density is ρ_w and drag coefficient is C_w. Ocean current is neglected.

The modal coefficients are related by the vector ordinary differential equation

$$m\frac{d\left(i\overline{\mathbf{v}}\right)}{dt}+\mathbf{b}'\cdot\left(i\overline{\mathbf{v}}\right)+\left(\frac{k}{L}\right)\overline{\boldsymbol{\sigma}}\cdot\mathbf{n}=\mathbf{0}\,, \tag{12}$$

where the applied body force $\hat{\boldsymbol{\tau}}$ is ignored because we seek non-trivial solutions to the homogeneous equations.

Elastic-Plastic Constitutive Law Perturbation Equation

It is customary in solid mechanics (e.g., *Schreyer*, 2001) to neglect the dependence of $\mathbf{M}_{ep}$ on the stress tensor. Substituting the normal modes for velocity and stress gives

$$\frac{d\,\overline{\boldsymbol{\sigma}}}{dt}=\left(\frac{k}{L}\right)\mathbf{M}_{ep}:\left(\mathbf{n}\otimes i\overline{\mathbf{v}}\right), \tag{13}$$

since the strength modulus term in equation (7) is zero for the three cases analyzed here. Symmetry of the elastic-plastic modulus with respect to its last two indices allows us to avoid writing the full symmetric form for $\overline{\mathbf{D}}$.

Since the stress modal coefficient appears in the momentum balance perturbation equation (12) only in the combination $\overline{\boldsymbol{\sigma}}\cdot\mathbf{n}$, we can form that term as

$$\frac{d\left(\overline{\boldsymbol{\sigma}}\cdot\mathbf{n}\right)}{dt}=\left(\frac{k}{L}\right)\mathbf{A}_{ep}\cdot\left(i\overline{\mathbf{v}}\right), \tag{14}$$

where

$$\mathbf{A}_{ep}=\mathbf{n}\cdot\mathbf{M}_{ep}\cdot\mathbf{n}\,, \tag{15}$$

is the elastic-plastic acoustic tensor. Symmetry of the first two indices of $\mathbf{M}_{ep}$ allows us to write the tensor in this form.

Differentiating equation (12) with respect to time and substituting equation (14), we can rewrite the ordinary differential equations in terms of the velocity modal coefficient as

$$m\frac{d^2\left(i\overline{\mathbf{v}}\right)}{dt^2}+\mathbf{b}'\cdot\frac{d\left(i\overline{\mathbf{v}}\right)}{dt}+\left(\frac{k}{L}\right)^2\mathbf{A}_{ep}\cdot\left(i\overline{\mathbf{v}}\right)=\mathbf{0}\,. \tag{16}$$

We note that the solution state is assumed constant for the stability analysis. This equation has solutions of the form

$$\overline{\mathbf{v}}\left(t\right)=\mathbf{v}_0e^{-\kappa t}\,, \tag{17}$$

where $\mathbf{v}_0$ are coefficients of the initial perturbation, and decay rate κ is the negative of the Lyapunov coefficient. Comparing equations (9) and (17) shows that the initial perturbation has been expanded in the trigonometric series $\mathbf{v}_0e^{ik\mathbf{n}\cdot\mathbf{x}/L}$. The same eigenvectors are found for the traction $\overline{\boldsymbol{\sigma}}\cdot\mathbf{n}$.

Elastic-Plastic Characteristic Equations

The characteristic polynomial results from substituting equation (17) into (16) and setting the determinant of coefficients to zero. Thus,

$$\left| m\kappa^2 \mathbf{1} - \mathbf{b}'\kappa + \left(\frac{k}{L}\right)^2 \mathbf{A}_{ep} \right| = 0 . \tag{18}$$

This characteristic equation is a fourth order polynomial in κ. Since coefficients are real, roots must be real or complex conjugate pairs. We evaluate roots numerically for a full range of values of each parameter. For large wave numbers ($k \to \infty$), the acoustic tensor term dominates the body force term. Then the decay rate is proportional to *k* and determined from the eigenvalues of the acoustic tensor.

Three Special Cases

We analyze the three constitutive laws: elastic, elastic-plastic on the tensile cutoff cone, and stress at the origin. These cases represent the beginning steps for analyzing a complete EP model.

Stress States within Yield Surface (Elastic). The perturbation to equation (5) is (replace elastic strain rate with the stretching tensor when elastic)

$$\frac{d\hat{\sigma}}{dt} = \left(M_I - M_{II}\right)\hat{D}_I \mathbf{1} + 2M_{II}\hat{\mathbf{D}} . \tag{19}$$

Substituting normal modes and expanding their derivatives give

$$\frac{d\left(\bar{\boldsymbol{\sigma}}\cdot\mathbf{n}\right)}{dt} = \left(\frac{k}{L}\right)\left[M_I \mathbf{n}\otimes\mathbf{n} + M_{II}\mathbf{1}\right]\cdot\left(i\bar{\mathbf{v}}\right). \tag{20}$$

Thus, by equation (14) the elastic acoustic tensor is

$$\mathbf{A}_e = M_I \mathbf{n}\otimes\mathbf{n} + M_{II}\mathbf{1} . \tag{21}$$

This form can be used directly in the characteristic polynomial. The eigenvalues of $\mathbf{A}_e$ are $M_I + M_{II}$ and M_{II}. Thus, if body forces are neglected ($\mathbf{b}' = \mathbf{0}$), then roots of the characteristic polynomial are $\kappa = \pm i\sqrt{\left(M_I + M_{II}\right)/m}$ and $\kappa = \pm i\sqrt{M_{II}/m}$, which is the desired classical mechanics result. Since they are purely imaginary, the modes propagate at the dilatational and shear wave speeds without decay.

The zero mode (*k*=0) is not affected by the constitutive law. Two roots are zero, and two are complex conjugates that depend on ice speed. The real part of the nonzero roots satisfies

$$m\,\mathrm{Re}\left(\kappa\right) = \frac{3}{2}\rho_w C_w \,|\,\mathbf{v}\,|\cos\beta . \tag{22}$$

They are positive so the zero mode is stable.

In Figure 2 real parts of the characteristic roots for the first elastic mode ($k = 1$) are shown. They are positive and the mode is stable. For all cases analyzed here, we have plotted the real parts of all roots versus ice speed. At each speed, we have calculated the roots as functions of velocity direction δ and the orientation vector direction α. Many,

if not most, of these solutions are identical. Only a few distinct values at each speed appear in the solutions. All roots near zero are in fact positive as can be seen by applying the Routh-Hurwitz Condition (e.g., *Fisher*, 1999).

As the mode number increases to k=10, two pairs of complex conjugate roots exist (Figure 3). Both are always positive so the mode is stable. These roots approach each other because the body force term in equation (18) is smaller than the inertia or the acoustic tensor term. As k increases, the complex conjugate pairs approach each other, and all real parts become identical.

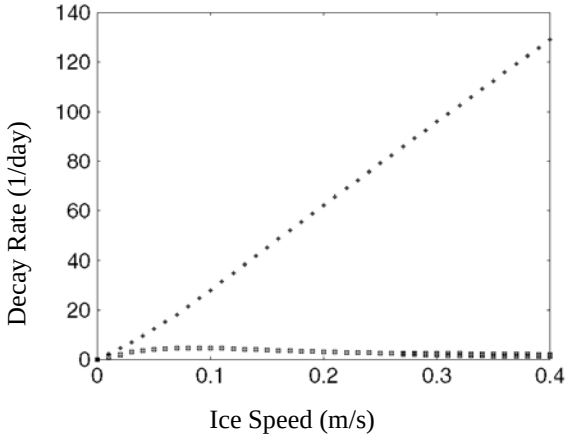

Fig. 2. Real root parts for first elastic mode (k=1)

For zero velocity of all modes, the linear and cubic coefficients are zero. This case fails the Routh-Hurwitz Condition, but the characteristic polynomial reduces to a quadratic polynomial in κ^2. The square root of any complex (or real) number must be mapped into the positive half of the complex plane, so the desired roots κ must have positive real parts. Thus, the elastic model is stable. When ice speed is not zero, the characteristic polynomial satisfies the Routh-Hurwitz Condition so all roots are positive.

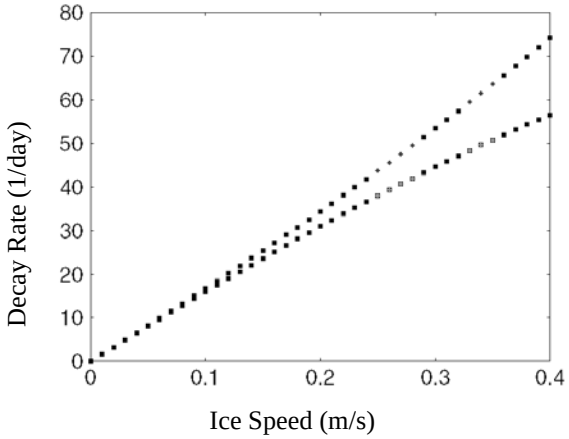

Fig. 3. Real root parts for tenth elastic mode (k=10)

Stress States on Tensile Cutoff Cone. On the tensile cutoff cone, the stress state satisfies

$$\phi = \sigma_{II} + \sigma_I \,, \tag{23}$$

which is independent of strength p*. This precludes the stress state from being at the shearing corner because opening there would cause weakening and dependence on $p*$. For the present analysis, we simply assume that ϕ is independent of strength.

The elastic-plastic modulus can be derived for isotropic yield surfaces by using equation (3) and (5) and the fact that, for the tensile cutoff cone, the partial derivatives are

$$\frac{\partial \phi}{\partial \boldsymbol{\sigma}_I} = \frac{\partial \phi}{\partial \boldsymbol{\sigma}_{II}} = 1. \tag{24}$$

Thus, for these stress states

$$\mathbf{M}: \frac{\partial \phi}{\partial \boldsymbol{\sigma}} = M_I \mathbf{1} + M_{II} \frac{\boldsymbol{\sigma}'}{\sigma_{II}} \tag{25}$$

After substituting the elastic-plastic modulus into equation (15) and using (25), the EP acoustic tensor becomes

$$\mathbf{A}_{ep} = \mathbf{A}_e - \frac{\mathbf{T} \otimes \mathbf{T}}{M_I + M_{II}}, \tag{26}$$

where

$$\mathbf{T} = (M_I + M_{II})\mathbf{n} + M_{II} \frac{\boldsymbol{\sigma} \cdot \mathbf{n}}{\sigma_{II}}. \tag{27}$$

The vector **T** depends only on the direction of principal stress γ through $\boldsymbol{\sigma} \cdot \mathbf{n} / \sigma_{II}$ and the unit length orientation vector **n**. Therefore, roots of the characteristic polynomial (18) depend on velocity **v** through $\mathbf{b}'$, direction of principal stress, orientation vector direction, mode number k/L, and material properties such as elastic moduli M_I and M_{II} and mass density *m*.

The zero plastic mode is the same as the elastic case, which has perturbation roots given by equation (22). Roots of the first elastic-plastic mode is presented in Figure 4. Although there are more distinct roots, the general trends are similar to the first elastic mode shown in Figure 2. The real parts of all roots are positive so the mode is stable. For the tenth plastic mode, roots are presented in Figure 5. This mode is more complicated than any presented previously, but the crucial fact is that all roots have positive real parts. As with the elastic cases, all plastic modes satisfy the Routh-Hurwitz Condition. Thus, roots near zero are positive. When ice speed is zero, two coefficients are zero, which violates the Routh-Hurwitz Condition, but a separate analysis proves this case to have positive roots. Thus, all plastic modes are stable.

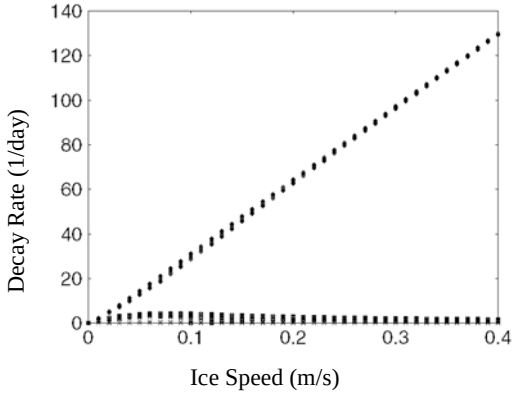

Fig. 4. Real root parts for first plastic mode (*k*=1)

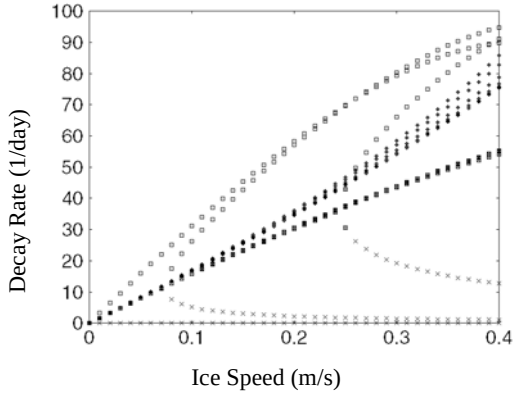

Fig. 5. Real root parts for tenth plastic mode (*k*=10)

Stress State at the Origin. When stress is at the origin ($\boldsymbol{\sigma} = \mathbf{0}$) for a finite period, it also has zero stress rate ($\dot{\boldsymbol{\sigma}} = \mathbf{0}$). Thus, from equation (4), the elastic strain rate is zero ($\dot{\mathbf{e}} = \mathbf{0}$), and from equation (6), still neglecting rigid body rotations, $\mathbf{D}_p = \mathbf{D}$. If we combine all equations into the single rate equation, the elastic-plastic modulus to be zero ($\mathbf{M}_{ep} = \mathbf{0}$). The acoustic tensor given by equation (15) is also zero ($\mathbf{A}_{ep} = \mathbf{0}$). The model is therefore the same as the zero mode, which has perturbation roots given by equation (22). These complex roots imply that the perturbations oscillate in time, but the decaying real part ensures stability.

CONCLUSION

We have showed that an EP model is stable if the yield surface is described by a tensile cutoff cone. This is one step toward learning if the EP model is stable for all solution states. We have begun this study by focusing on the tensile cutoff cone because plastic failure during opening is the condition most likely to be unstable. More work is needed to analyze the EP models when stress is on the compressive cap and strength can change during the deformation. That analysis will require that strength be included in the set of variables, increasing the dimension of the solution perturbation space. We should also include effects of allowing the elastic-plastic modulus $\mathbf{M}_{ep}$ to vary as a function of stress, which also increase the dimension of the solution perturbation space because three stress components must be included.

ACKNOWLEDGMENTS

This work was supported by IR&D funds from IceCasting, Inc. I thank Prof. K. M. Dempsey, Clarkson U., for alerting me to the Routh-Hurwitz Condition.

REFERENCES

Coon, M.D., Maykut, G.A., Pritchard, R.S., Rothrock, D.A., and Thorndike, A.S. Modeling the pack ice as an elastic-plastic material, in *Aidjex Bulletin*, U. Wash., Seattle (1974) 1-105.

Drucker, D.C., A definition of stable inelastic material, *J. Appl. Mech.*, *26*: 101-106 (1959).

Fisher, S.D., Complex Variables, 2nd ed., *Dover*, Mineola, NY (1999) 427 p.

Gray, J.M.N.T., Loss of hyperbolicity and ill-posedness of the viscous-plastic sea ice rheology in uniaxial divergent flow, *J. Phys. Ocean.*, *29*: 2920-2929 (1999).

Gray, J.M.N.T., and Killworth, P.D., Stability of the Viscous-Plastic Sea Ice Rheology, *J. Phys. Oceanogr.*, *25*: 971-978 (1995).

Hibler, W.D., III, A dynamic thermodynamic sea ice model, *J. Phys. Ocean.*, *9* (4) (1979) 815-846.

Pritchard, R.S., An Elastic-Plastic Constitutive Law for Sea Ice, *J. Appl. Mech.*, *42* (E2) (1975) 379-384.

Pritchard, R.S., Mechanical behavior of pack ice, in Mechanics of Structured Media, A.P.S. Selvadurai (ed), *Elsevier*, Amsterdam (1981) 371-405.

Pritchard, R.S., Ice Conditions in an Anisotropic Sea Ice Dynamics Model, *Int'l. J. of Offshore and Polar Engineering*, *8* (1) (1998) 9-15.

Pritchard, R.S., Stability of Sea Ice Dynamics Models, in Ice in the Environment: *Proceedings of the 16th IAHR International Symposium on Ice*, V. Squire and P. Langhorne (eds), *IAHR*, Dunedin, NZ (2002) 391-398.

Pritchard, R.S., Stability of Quasi-Steady Viscous-Plastic Ice Models, in *POAC'03*, S. Løset (ed) Trondheim, Norway, (2003) 83-92.

Pritchard, R.S., Stability of Sea Ice Dynamics Models: Viscous-Plastic Rheology, Replacement Closure and Tensile Cutoff, *J. Geophys. Res*. (2004 accepted).

Pritchard, R.S., Reimer, R.W., and Coon, M.D., Ice Flow through Straits, in *Proceedings of POAC79*, Vol.3, Trondheim, Norway, (1979) 61-74.

Schreyer, H.L., Modeling failure initiation in sea ice based on loss of ellipticity, in Scaling Laws in Ice Mechanics and Dynamics, J.P.Dempsey and H.-H. Shen (eds), *Kluwer*, Dordrecht, (2001) 239-250.

17th International Symposium on Ice
Saint Petersburg, Russia, 21-25 June 2004
International Association of Hydraulic Engineering and Research

NUMERICAL MODELLING OF ICE INTERACTION WITH RUBBLE MOUND BERMS IN THE CASPIAN SEA

A. Barker[1] and K. Croasdale[2]

ABSTRACT

Numerical modelling of sea ice is a useful tool in predicting ice rubble formation around offshore and coastal structures. Such models can capably predict rubble height and extent, allowing engineers to pinpoint "problem" scenarios for structures where ice interaction, and its potential for extensive damage, is a concern. This paper describes numerical simulations that were conducted to examine floating ice interaction with a structure located in the Caspian Sea and its planned surrounding protective rubble mounds. Spatial and temporal distributions of ice rubble pile-up height and depth, as well as forces on the mounds, were determined. The numerical model examined a number of different rock mound configurations, the influence of the direction of ice movement and ice sheet thickness. The results are compared with reported pile-up heights, collected from the field site.

INTRODUCTION

This objective of this paper is to summarize the findings of a numerical model that was used in conjunction with field work and laboratory tests to examine design options for a drilling site in the Caspian Sea. The paper also gives an overview of full-scale conditions for comparison purposes. The numerical model examined floating ice interaction with a barge-type structure and the rock mounds that were to be constructed around it, as part of a contract that the Canadian Hydraulics Centre (CHC) of the National Research Council of Canada carried out for the Agip Kazakhstan North Caspian Operating Company NV (AGIP KCO, formerly OKIOC) (Sayed and Barker, 2000). The problem that was to be studied corresponded to design options for an exploration-drilling structure in the Kazakhstan sector of the north Caspian Sea (see Figure 1).

The structure, called the Sunkar, is 85 m by 55.5 m. Rubble mounds, along the long axis, were at one point considered as protection for the Sunkar from moving ice, although this layout was subsequently discarded. Numerical simulations were conducted in order to determine, for each design option, the expected ice pileup geometries, ice

[1] Canadian Hydraulics Centre, National Research Council of Canada, Ottawa,ON, K1A 0R6 Canada
[2] K.R. Croasdale & Associates Ltd., 2120, 720, 13th Avenue S.W. Calgary, AB, Canada T2R 1M5

rubble grounding, and forces on the rock mounds and structure. Several options for the layout and dimensions of the mounds were examined. The data from these simulations were then compared with ice measurements taken the following season by K.R. Croasdale and Associates, in response to a tender issued by AGIP KCO for an ice research and measurement programme for the North Caspian Sea (Croasdale, 2001).

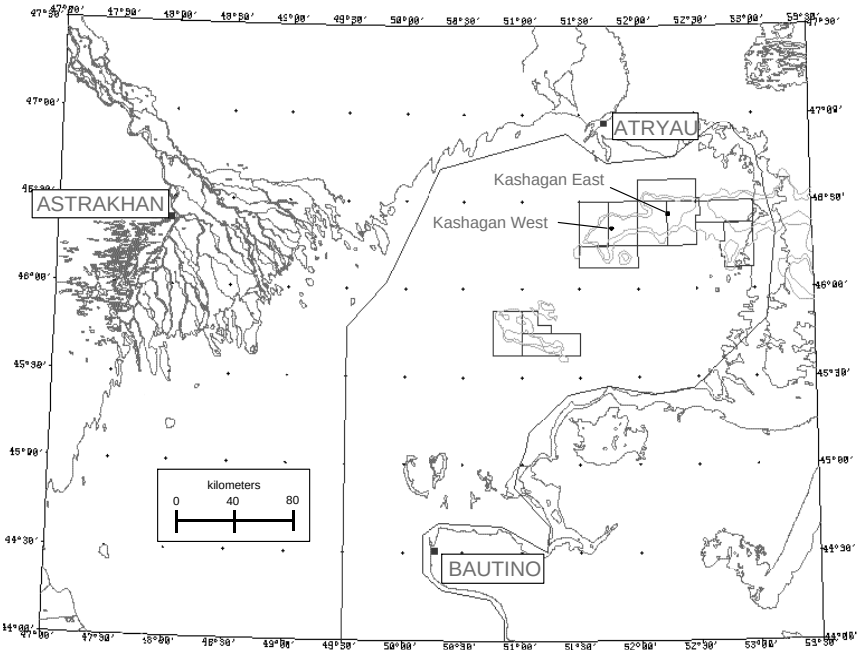

Fig. 1. Regional map of Caspian Sea (from Croasdale, 2001)

PARTICLE-IN-CELL NUMERICAL MODEL

Model Description

A Particle-In-Cell (PIC) numerical model developed at the CHC has been used successfully to deal with a number of ice-structure interaction issues (Sayed et al., 2000; Barker et al., 2000; 2001a; 2001b). The numerical model uses a continuum rheology that follows a Mohr-Coulomb plastic yield criterion. An assembly of discrete particles represents the ice cover. The governing equations consist of the continuum equations for the balance of linear momentum and the plastic yield criterion. Those equations are solved using a fixed grid. Advection and continuity, on the other hand, are handled in a Lagrangian manner. An implicit finite difference method is used, based on uncoupling the velocity components and a relaxation iterative scheme. Each particle has a fixed volume, and is assigned an area and a thickness. At each time step the velocities are interpolated from the grid to the particles. Thus, particles can be individually advected. From the new positions, values of particle area and mass are mapped to the grid. The resulting ice mass and area for each grid cell are then used to update ice thickness and concentration. Solution of the governing equations can then be carried out using the fixed grid. Updated velocities and stresses on the fixed grid are obtained from the solution. Both three dimensional and depth-averaged implementations of the model were used in this paper; the latter averages the values of stresses and velocities over the thickness. Thickness variations, however, are accounted for. As stresses exceed a threshold, representing a ridging stress, each particle undergoes ridging; i.e. the thickness increases and area

decreases, while conserving ice volume. Further details about the model may be found in Sayed and Carrieres, 1999.

Test Set-Up

The numerical model was used to investigate floating ice interacting with the Sunkar, and its surrounding protective rubble mounds. The simulations that were performed for AGIP KCO consisted of two base cases each with sensitivity and three-dimensional runs. The first base case looked at one rubble mound along the east side of the structure, and another mound along the west side of the structure. For the second base case, two mounds (separated by a gap) were placed along the east and west sides of the structure. Figure 2 shows the general layout. Runs were conducted using different values for the direction of ice movement, distances between the structure and mounds, and gap between the mounds. The effects of changing the freeboard and width of the mounds were also examined. The output of each run gave the extent and spatial distribution of rubble pileup sail height and keel depth in front of the mounds and the structure. The spatial distribution of grounding was also given. The forces on the mounds and the structure were determined. Overall, thirty-three runs were completed.

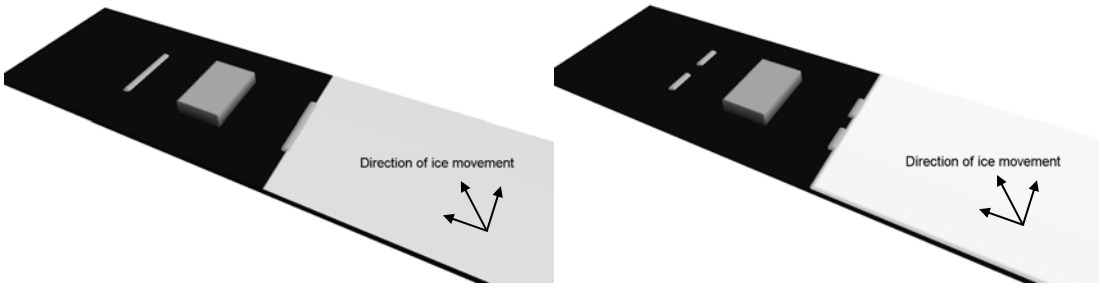

Fig. 2. General test layout for the test cases. The second case (right) had two mounds on either side of the barge, with a gap of various widths, rather than the single berm of the first case (left)

The ice thickness used in the runs was usually either 0.05 m or 0.15 m. These relatively small thickness values were chosen as the predominant thickness during the freeze-up, when it was anticipated that most of the pile-up activities would take place. The ice had a constant ice velocity of 0.5 m/s. The water depth was 4 m, with a 1 m freeboard for the rubble berms. The rubble berms were to have 1:3 slopes (18° from horizontal). An angle of internal friction of 30° was appropriate for modeling the depth-averaged behaviour (as established in previous studies; e.g. Sayed et al. 2000). A number of boundary conditions were used, depending upon the test run configuration. The boundary conditions could include full-slip (ice velocity parallel to the boundary), prescribed velocity (to drive the ice cover) or stress-free (used downstream of a structure) conditions. The environmental driving force on the ice sheets was applied via a water drag coefficient, between 0.5 and 1.5 depending on the ice thickness. The lower value corresponds to a maximum applied shear stress of approximately 1.25 kPa exerted on stationary parts of the ice cover. These values are in accordance with observations of ice jams (Beltaos, 1995). Overtopping of the rubble mound structures was not permitted, although additional tests did examine this scenario. Those simulations showed that ice pileup would not overtop a mound with 1 m freeboard. For a lower freeboard of 0.5 m, a pileup would spill some ice rubble on the top of the mound, but all rubble is stopped in front of the mound. Therefore, the structure remained protected.

Summary of test results

The spatial distribution of ice rubble pileup showed that almost all of the pileup occurs against the East mound (Figure 3). The structure and West mound were sheltered from the ice and forces there were negligible. Pileup against the East mound appeared to form in rings. Once a maximum thickness (height and depth) were reached, the pileup extended outwards, upstream. The pileup grounded on the slopes of the mound and seabed. Forces on the mounds were calculated by integrating the normal stresses acting directly on the mound and grounding shear stresses. The forces on the structure were calculated by integrating the normal stresses at its interface with the ice. The resulting maximum pressure of 2 kN/m is in accordance with observations (Masterson, 2000). The total force on the mound was approximately 90 kN, which was, as expected, relatively low. For a quantitative description of the pileup, the sail height and keel depth were plotted along several cross-sections; an example is shown in Figure 4. The sensitivity runs for Case 1 gave quantitative estimates of the effects of changing ice direction, mound length, and separation distance between the structure and the mound. The direction of ice movement obviously influenced the effectiveness of rubble mounds to protect the structure. The effect of the separation distance became pronounced with increasing angle of ice movement direction. The larger separation exposed the structure to more ice action. Increasing the length of the mound increased the protection of the structure, particularly for oblique angles of ice approach and larger separation distances.

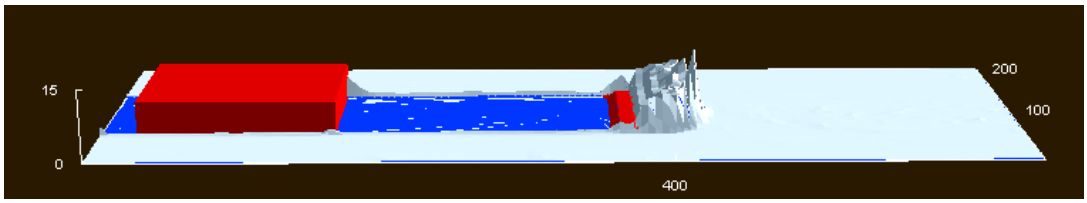

Fig. 3. Ice interacting with a rubble berm. The Sunkar is on the left hand side

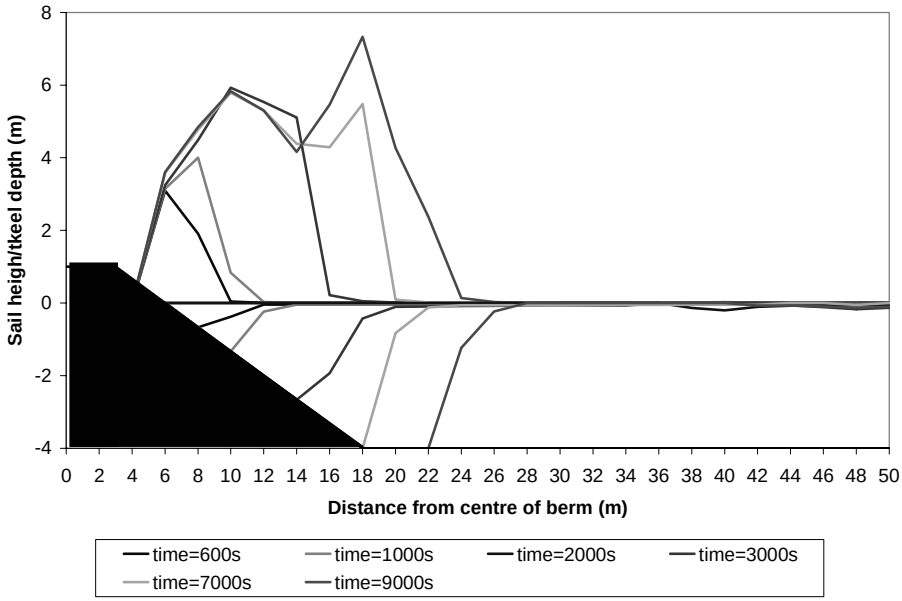

Fig. 4. Cross-sectional view of development of sail and keel thicknesses over time. Note the grounding and steep angle of repose

For the second case, at the early stages of the run, pileups formed in front of both East mounds. The ice sheet also passed through the gap between the mounds and a pileup

developed against the structure. As the pileup against the structure grew, it reached the gap, which eventually filled with grounded ice. Afterwards, a single grounded pileup developed in front of the both the East mounds. Once this occurred, the two adjacent mounds acted as a single large mound, which provided shelter for the structure. With a larger ice sheet thickness, the pileup formed and grounded in the gap between the mounds. For a larger separation distance between the mounds and the Sunkar, the pileup in front of the structure obviously took longer to reach the gap. Increasing the angle of ice movement (from the x-direction to an oblique angle) was shown to expose larger parts of the structure to ice action. Also, the gap between mounds appeared to block earlier. The latter result is expected since the projected gap width normal to ice movement would be smaller. The larger gap and the corresponding smaller mound length produced pileup in front of each mound and the structure. The larger separation distance exposed the structure to increased ice action. In cases where the gap was greatest, the gap did not become blocked. Additionally, a run was done to examine the stability of an existing grounded pileup under the action of a moving ice sheet. The results showed that the grounded pileups did not move under the action of the moving ice sheet. Instead, a new, grounded pileup formed on the South sides of the existing pileup and the structure. Only a small part of the initial pileup, west of the mounds, that was not firmly grounded was cleared by the moving ice sheet.

MEASURED FULL-SCALE FEATURES

The full-scale data was collected in February 2001 (Croasdale, 2001). The main focus of the project was to examine grounded ice rubble and ridge features. The measurements that were collected that pertain to this paper included ridged and rafted ice thickness and geometry, ice pile-up geometry and block size distribution and other measurements concerning sea water and ice properties. Overall, fourteen features were surveyed over the course of the month. General descriptions for each feature are shown in Table 1. With respect to the ice conditions in the area of the drill site, ice is generally present from December to March, with a mean level ice thickness ranging between 0.3 m to 0.5 m. The water depth is quite shallow (the water depth in the study area is 4 m), with a deepest depth of approximately 10 m. Ice ridging and rafting occur frequently in the area, with keels scouring the seabed in the case of the former. A photograph of one of the features is shown in Figure 5. Table 1 lists the sail and keel measurements, water depth and level ice thickness for each feature, as well as some other pertinent details, where available. Feature 14 is omitted, as it was a sounding at various locations. The average sail (pile-up) height of the observed features was 3.3 m, with a maximum height of 6.6 m. The average thickness of the surrounding ice sheet was 0.33 m. The water depth varied from 2.0 to 5.9 m, and most of the features had grounded on the seabed. Croasdale (2001) discussed that it appeared that ice pile ups in the Caspian could be higher than other regions (for the same ice thickness), which he attributed to the shallower water and reduced ice friction between ice blocks due to lack of snow.

COMPARISON WITH FULL-SCALE DATA

A direct comparison between the full-scale data and the numerical results is difficult, given that most of the full-scale features were not generated due to interaction with a structure such as the Sunkar. Nevertheless, it is possible to compare the results by examining the relationship between the surrounding level ice thickness and the generated pile-up height. Figure 6 shows two views of ice that did, however, interact with the protective piles that were used at one point to shield the Sunkar. As can be seen in this figure

and Figure 5, the pile-ups could be quite steep. This was also observed in the numerical results, as shown in Figure 4.

Fig. 5. Photo of typical feature surveyed in the Caspian Sea (Croasdale, 2001)

Table 1. Details of full-scale features surveyed in Caspian Sea (after Croasdale, 2001)

Feature Number	**Feature Length**	**Feature Width**	**h_{sail}**	**h_{keel}**	**h_{water}**	**$h_{level\ ice}$**	**Dominant ice thickness at pile-up**	**Comments**
	m	**m**	**m**	**m**	**m**	**m**	**m**	
1	na	na	3.0	na	2.0	0.23		Rubble pile
2	150	50	6.6	2.6	2.6	0.35	0.30	Grounded ridge/rubble pile
3	30	25	3.0	2.5	2.5	0.32		Rubble pile within 1 km of Feature 2
4a	80	20	3.2	2.0	2.0	0.35		Series of ridges
4b	50	20	3.6	2.0	2.0	0.35		Series of ridges
5	na	na	3.2	3.5	3.5		0.13	Series of ridges
6	na	na	3.7	3.5	3.5		0.19	Series of ridges
7	na	na	1.6	3.7	3.8	0.40	0.16	Series of ridges
8	na	na	na	na	na	0.38		Sonar survey south of (east) piles
9	90	60	5.5	4.3	4.3		0.20	Exposed rock berm
10	30	10	2.1	2.0	2.0		0.07	Rubble pile near Aktote
11	10	10	0.5	2.0	2.0	0.3		Rafted ice/floating ridge area
12	>1000	50-200	5.6	5.9	5.9		0.17	Newly formed grounded ridge and rafted ice ~ 8km from Sunkar
13	65	50	0.5	5.8	5.8	2-3 (rafted)		Rafted ice floes in front of ridge
14								Ice thicknesses and soundings on line from Aktote to shore

Croasdale (2001) plotted the relationship between the ice thickness and the pile-up height for a number of the surveyed features (Figure 7). The plot shows good correlation between dominant ice thickness and pile-up height. A similar chart was created that included data points from a large number of geographic areas, as well as the Caspian full-scale and numerical results. This plot is shown in Figure 8. The Caspian data is on

the low-end of the measured ice thickness data. In this region, it can be seen that there is a moderate amount of scatter in the pile-up heights encountered with thin ice. However, both the full-scale and the numerical results fall in with data from other geographic regions. Note that there are numerous pile-up thicknesses for the numerical results for each ice thickness, due to multiple test runs with different configurations in the parametric study.

SUMMARY

The preceding paper describes ice rubble pileup geometries and forces due to an ice sheet impinging on a structure protected by arrangements of rock mounds, and the associated full-scale data for comparison purposes. The chosen driving force and material parameters produced the expected pileup thickness. The maximum grounded thickness was approximately 10 m, with a corresponding pileup height of 6 m in 4 m of water. This result is in agreement with the range observed in the Caspian (Spring, 2000, Croasdale, 2001), and other locations in the Arctic under relevant conditions.

ACKNOWLEDGMENTS

The authors wish to acknowledge Michel Metge, of AGIP-KCO, for obtaining permission to use the full-scale data as well as the assistance of Walt Spring, Exxon Mobil Upstream Research and Dr. Mohamed Sayed, Canadian Hydraulics Centre.

Fig.6. Two views of pile-up occurring at piles used to shelter the Sunkar drilling barge (Croasdale, 2001)

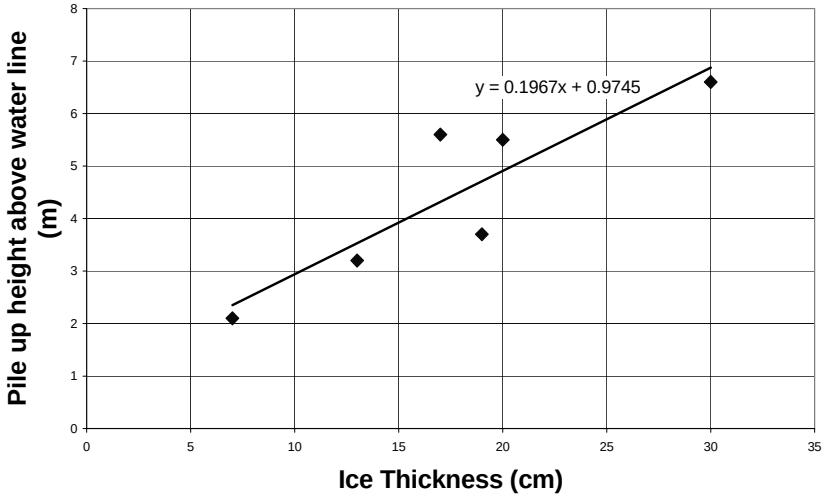

Fig. 7. Pile up height versus ice thickness (Croasdale, 2001)

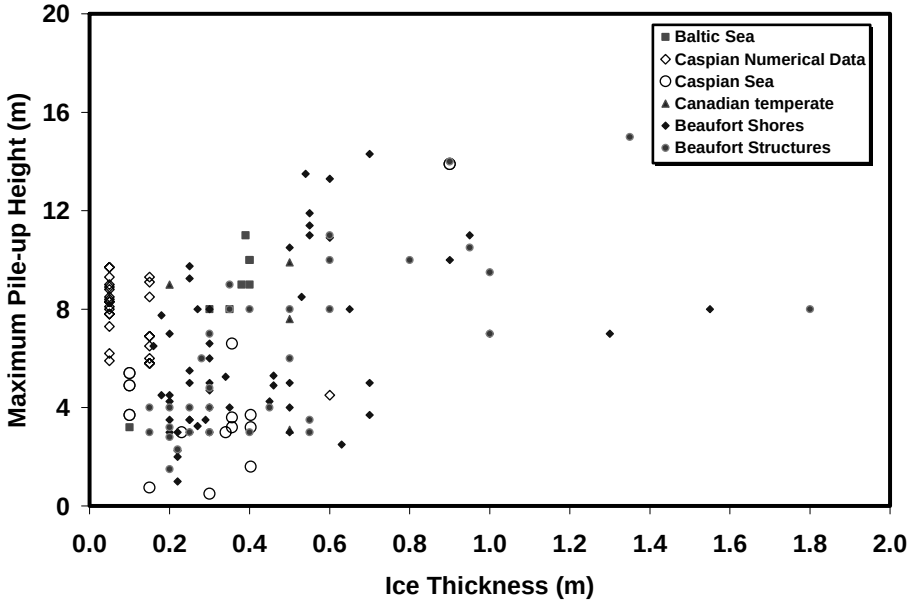

Fig. 8. Maximum pileup height versus thickness for full-scale and model data

REFERENCES

Barker, A., Timco, G. and Sayed, M. (2001a) Three-Dimensional Numerical Simulation of Ice Pile-Up Evolution Along Shorelines. *Proceedings of the 2001 Canadian Coastal Conference*. pp167-180. Laval, Canada.

Barker, A., Timco, G. and Sayed, M. (2001b) Numerical Simulation of the Broken Ice Zone Around the Molikpaq: Implications for Safe Evacuation. *Proceedings of the 16th Conference on Port and Ocean Engineering under Arctic Conditions.* Vol.2, pp 505-515, Ottawa, Canada.

Barker, A., Timco, G. Sayed, M. and Wright, B.D. (2000) Numerical Simulation of the "Kulluk" In Pack Ice Conditions. *Proceedings of the 15th IAHR Symposium on Ice*. Vol.1, pp 165-171, Gdansk, Poland.

Beltaos, S. (1995). River Ice Jams, *Water Resources Publications*, 372 pages.

Croasdale, K. (2001) Final Report Ice Research & Field Measurement Programme North Caspian Sea. Confidential report prepared for Offshore Kazakhstan International Operating Company (now AGIP KCO). Calgary, Canada.

Masterson, D. (2000). Personal communication.

Sayed, M., and Barker, A. (2000) Computer Modeling of Ice Interaction with Rock Mounds. Canadian Hydraulics Centre Confidential Report HYD-CTR-093. Ottawa, Canada.

Sayed, M., and Carrieres, T. (1999) Overview of a New Operational Ice Forecasting Model, *Proceedings of the 9th International Offshore and Polar Engineering Conference*. Vol. II, pp.622-627. Brest, France.

Sayed, M., Frederking, R., and Barker, A. (2000) Numerical Simulation of Pack Ice Forces on Structures: a Parametric Study. *Proceedings of the 10th International Offshore and Polar Engineering Conference*. Vol.1, pp.656-662. Seattle, USA

Spring, W. (2000). Personal communication.

Spring, W. (1997) 1997 North Caspian Ice Field Program. *OKIOC report*. 97-36-1-0

Timco, G. and Barker, A. (2002) What is the Maximum Pile-Up Height For Ice? *Proceedings of the 16th IAHR Symposium on Ice*, Vol. 2, pp 69-77, Dunedin, New Zealand.

17th International Symposium on Ice
Saint Petersburg, Russia, 21-25 June 2004
International Association of Hydraulic Engineering and Research

MODELLING ICE RUBBLE WITH PSEUDO-DISCRETE CONTINUUM MODEL

S. Shafrova[1,2], P. Liferov[2,3] and K. Shkhinek[4]

ABSTRACT

A pseudo-discrete continuum model was developed to study the breakage of the initial rubble skeleton. A special program was developed to generate a random assembly of rectangular blocks in a closed shape allowing to vary the block size and the resulting porosity of the assembly. The obtained assemblies were further used as geometrical input for the finite element model. The blocks were modelled as elasto-plastic bodies, contact elements were used to simulate the reduced strength at contacts between the blocks. Direct shear test simulation on the ice rubble were performed. The effect of the mechanical properties of the ice blocks and their contacts was investigated by applying different boundary conditions to assembly of the blocks.

INTRODUCTION

Several testing program on ice rubble mechanical properties have been done. Both laboratory and in-situ tests were performed. The results by Ettema and Urroz (1989, 1991) and Timco and Cornet (1999) confirmed that it is possible to describe ice rubble behaviour by elastic-perfectly plastic model, i.e. Mohr-Coulomb yield criteria.

Several methods to estimate the loads from ice ridges on offshore structures have been developed, both analytical and numerical models.

In the analytical approach the major difficulties are connected with the two-parametric Mohr-Coulomb failure criterion. The material properties (friction and cohesion) are not easy to determine. The cohesion term is mainly a function of freeze bonds between the ice blocks. Such bonds are broken at the initial stage in any interaction (Urroz and Ettema, 1989). The full frictional component cannot be mobilized until significant motion on failure plane has taken place. Thus, it is unlikely that frictional and cohesion terms

[1] University Centre on Svalbard, Longyearbyen, Norway
[2] Norwegian University of Science and Technology, Trondheim, Norway
[3] Barlindhaug Consult AS, Tromsø, Norway
[4] St. Petersburg State Polytechnical University, St. Petersburg, Russia

will act simultaneously. Several assumptions and simplifications were done and ice rubble was often treated either as frictionless or as cohesionless material.

Numerical approaches used Finite Element (FE) and Discrete Element (DE) models that can describe the behaviour of ice rubble. Recently only few FE based modelling was conducted by Heinonen, (2002, 2003) and Liferov et al., (2002, 2003). Punch tests were simulated in these models. The ice rubble was treated as a continuum and homogenous medium.

Discrete Element simulations by Hopkins and Hibler (1991) were done to study the behaviour and strength of ice rubble in the direct shear box. The freeze-bonding effect was neglected in these simulations. But it was suggested that a model of freeze-bonding might be used to explore various forms that such mechanism might take.

A pseudo-discrete continuum model, which simulates the initial breakage of the rubble skeleton, is described in this paper. The ice rubble was considered as discrete material and the effect of freeze bonds between individual ice blocks was taken into account. The model description and results of direct shear-box simulations are presented.

PSEUDO-DISCRETE CONTINUUM MODEL

General description

The pseudo-discrete continuum model of ice rubble is a combination of the discrete particle assembly generation (i.e. ice rubble accumulation) and the FE analysis of this assembly. The primary goal for developing such model was to study numerically the initial failure mechanism of ice rubble. This model provides a possibility to simulate the contacts between the ice blocks and their local failure.

The modelling procedure consists of two basic steps. First, the assembly of blocks is generated. The block generator tool was developed to fulfill this task. In the second step, the generated assembly is used as a geometrical input for the FE analysis to study its behaviour under loading at the different boundary conditions.

Generation of discrete block assembly

Generation of the discrete block assembly was conducted in the custom-developed computer program called the block generator. This program fills the closed contour with blocks of rectangular shape. The blocks themselves are considered as solid bodies. Geometry of each block is defined by its centre of gravity x_c, y_c and four vertices. The assumed porosity of assembly is used to calculate the number of blocks needed to fill the area. In the process of generation it is possible to define the area within a contour (by means of top and bottom control lines) to estimate its effective porosity. The direction of gravity is specified by the attraction line that can be given different locations within the contour throughout the simulation. Fig. 1 shows a typical interface view of the program during a simulation run. Detail description of the block generator is beyond the scope of this paper.

Finite element model

The generated assembly of ice blocks was used as a geometrical input for the FE analysis. It was conducted using the Plaxis FE code (Plaxis, 2002). The FE model of the ice rubble is shown in Fig. 2.

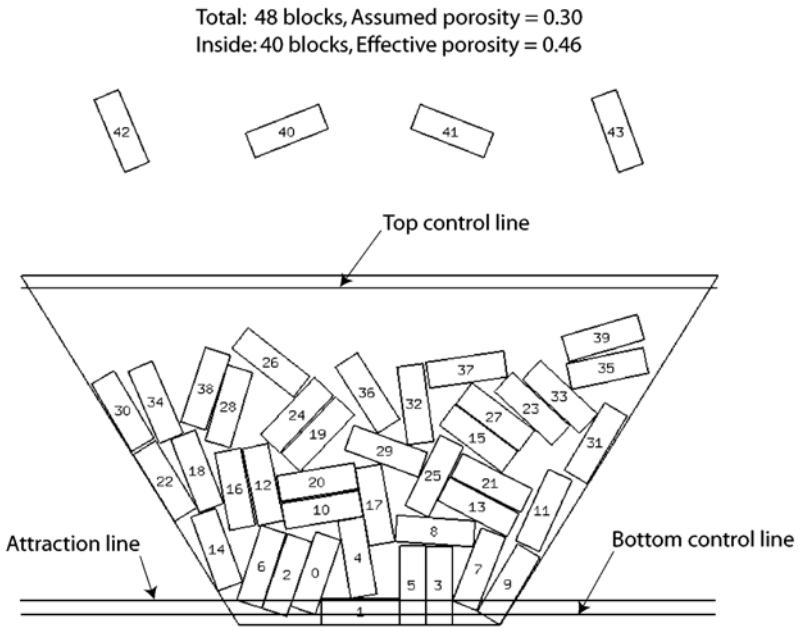

Fig. 1. Block generation in progress

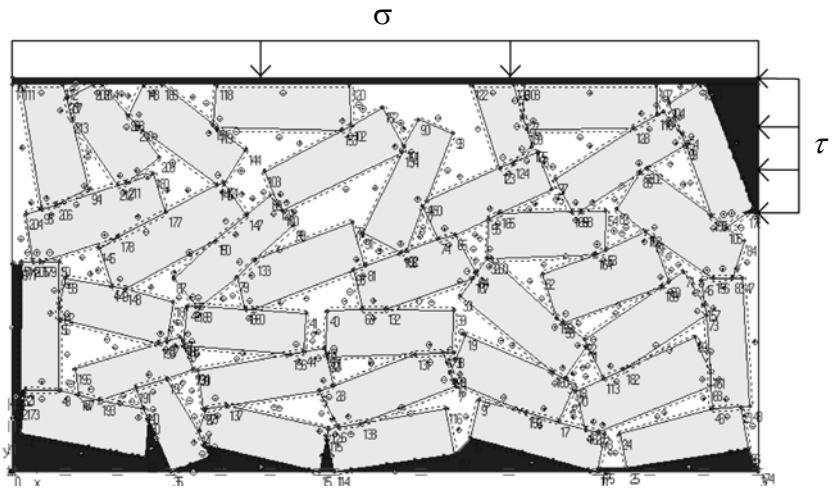

Fig. 2. The direct shear box
(σ is the normal pressure, τ is the horizontal pressure).

The model consists of:

The ice blocks. They were assigned an elastic-perfectly plastic Mohr-Coulomb material model. It is a constitutive model with a fixed yield surface, i.e. a yield surface that is not affected by plastic straining. The yield surface thus always coincides with the failure surface that is defined by six yield functions of the following form when formulated in terms of principal stresses σ_i, σ_j:

$$F = (\sigma_i + a) - N(\sigma_j + a), \tag{1}$$

where the following state parameters are used: $N = (1 + \sin\varphi) / (1 - \sin\varphi)$, φ is the angle of internal friction, a is the attraction ($a = c/\tan\varphi$), c is the cohesion. For $c > 0$, the standard Mohr-Coulomb criterion allows for tension. However, the ice normally sustains

smaller tensile stresses than those defined by the standard form of the failure criterion. In order to account for this, three additional yield functions are introduced:

$$F = \sigma_i - \sigma_t \text{ and } 0 \le \sigma_t \le a\,, \tag{2}$$

where σ_t is the tensile stress of ice.

The contacts between the blocks. They were modelled using the interface elements. Fig. 3 shows the close-up of contacts between ice blocks in the rubble (with the mesh on). The interface element shown in the figure to have a finite thickness, but in the FE formulation the coordinates of each node pair are identical, which means that the element has a zero thickness. Each interface has assigned to it a 'virtual thickness' which is an imaginary dimension used to define the material properties of the interface.

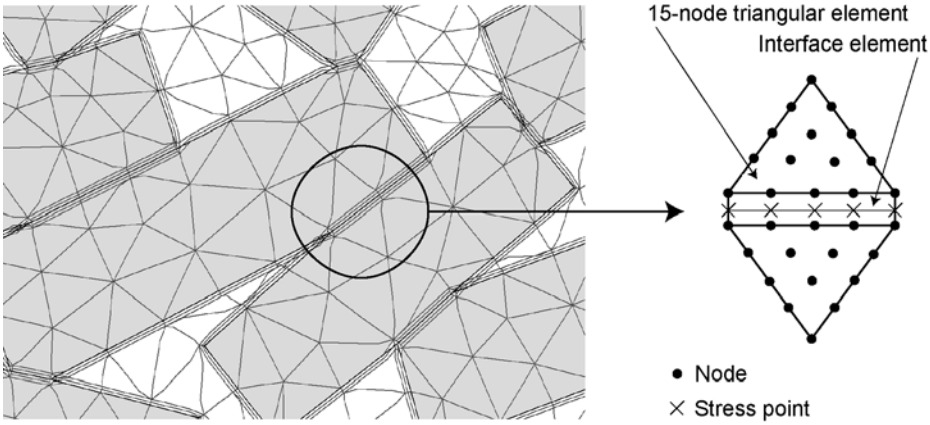

Fig. 3. Ice blocks in contact

The length of contacts between the blocks is assumed to be a variable parameter. For the initial step the contact length is established to have a minimum value which can sustain the applied load combination. In case of smaller values the material fails during construction stage under compression, which operated by normal pressure. Thus the contact lengths have to be increased for the further simulations.

The strength properties of the interfaces are linked to the strength properties of the ice blocks via the strength reduction factor for interfaces R_i as follows:

$$c_i = R_i \cdot c \text{ and } \tan\varphi_i = R_i \cdot \tan\varphi \tag{3}$$

The voids between the blocks. They were modelled using elastic material with a negligible stiffness. This was done to avoid mesh problems - use of elastic material instead of leaving voids "empty". Verification was conducted on identical models with and without elastic material in the voids to prove that it doesn't affect the results.

The quasi-static approach was used in the simulations. The ice rubble was modelled as a weightless material, i.e. initially the rubble was unloaded. Iterative calculations were carried out until the overall stiffness of the material approached zero (or resistance to loading began to decrease). This was an indication of complete breakage of the initial rubble skeleton.

NUMERICAL EXPERIMENTS

Direct shear box

The apparatus simulated in this set of numerical experiments is the two-dimensional direct shear box that is shown in Fig. 2. The inner length of the shear box is 6 m and the depth is 3 m. Load controlled deformation was applied to the upper part of material. The

lid was free to move vertically in order to balance the normal confining pressure σ applied to its upper surface. The horizontal pressure τ was then incrementally applied to move the upper part of the shear box. The ice rubble used in the experiments was made up of rectangular blocks. Table 1 presents the characteristic parameters for the ice blocks that were chosen according to Kämärinen, (1993).

Table 1. Ice block properties

Property	Value	Property	Value
Length, m	~ 1.0	Angle of internal friction, º	0-30 (var.)
Thickness, m	~ 0.3	Tensile strength, MPa	0.2
Young's modulus, GPa	4.5	Porosity, %	~ 33
Poisson's ratio	0.3	Amount of blocks,	~ 40
Cohesion, MPa	0.5		

Parametric analysis

A series of numerical tests were conducted with the direct shear box. The parametric study was performed in order to investigate the effect of mechanical properties of the ice blocks and their contacts on the strength of ice rubble skeleton. In addition the influence of normal pressure on the ice rubble strength was analyzed. The following parameters were assumed to be variable during the numerical experiments:

- strength reduction factor for interfaces - R_i;
- normal pressure – σ;
- angle of internal friction - φ;
- length of the contacts between ice blocks or contact area - A.

It was observed during simulation that initial failure of the ice rubble corresponds to breakage of the contacts between ice blocks. Therefore the initial strength is controlled by freeze bonding mechanism between separate blocks inside the ice rubble. The cohesion seems to be a major contributor to the bearing capacity of the ice rubble. Some local breakage of the individual ice blocks was also observed during simulations.

Influence of strength reduction factor

The shear strength τ versus strength reduction factor R_i for two different values of angle of internal friction is presented in Fig. 4. The normal pressure is assumed to be a constant and equal to 5 kPa.

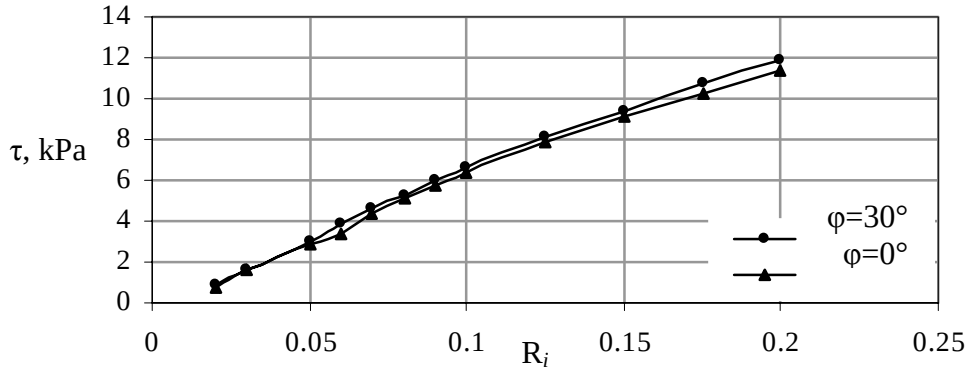

Fig. 4. Shear strength versus strength reduction factor, σ = 5 kPa

The shear strength increases almost linearly with increasing strength of the interface elements. It is clearly shown in Fig. 4 that initial failure is independent of φ. Thus strength of the ice rubble is largely dominated by cohesion and tensile strength of freeze-bonds.

Weiss et al. (1981) have proposed that effective cohesion of ice rubble, *c*, may be proportional to the thickness of ice blocks, t, which form the rubble. They indicated the following relationship: $c/t = 16 \pm 8\ kPa/m$. Bruneau (1997) conducted analysis of several ice rubble shear strength laboratory test and reported the following: $c/t = 17\ kPa/m$. In the following we assume the average c/*t* value is about 20 kPa/m. Thus for present simulations of 0.3 m thick ice blocks *c* is expected to be about 6-7 kPa.

Ettema and Schaefer (1986) conducted a series of experiments on freeze-bonding between ice blocks. They reported that the shear strength of freeze-bond is about 1-5 kPa for small-to-medium scale tests. The ice blocks with contact area of 4.52 x 10^{-3} m^2 and 9.03 x 10^{-3} m^2 were used during these experiments that correspond to 9.5 x 4.75 cm and 13.4 x 6.70 cm block size respectively. The scaling of these results coincides with simulation data in Fig. 4. The curves show that shear strength is in the range of 5-7 kPa for the strength reduction factor from 0.08 up to 0.1, that corresponds to 40-50 kPa for the freeze-bond shear strength.

Influence of contact area

Fig. 5 shows a plot of shear strength τ versus total contact area *A* between the ice blocks. The normal pressure is assumed to be a constant and equal to 5 kPa. The strength reduction factor is chosen as 0.09 that is a freeze bonding strength of 45 kPa.

For the range of contact area used in the present study, the shear strength of the ice rubble is linearly increased with increasing of contact area. The simulation indicated that length of contacts or contact area between ice blocks *A*, has a great influence on the shear strength. This prompts that results depend significantly on block size and position. Table 2 shows the typical values of the average length of the contacts between the ice blocks in relationship with the total contact area.

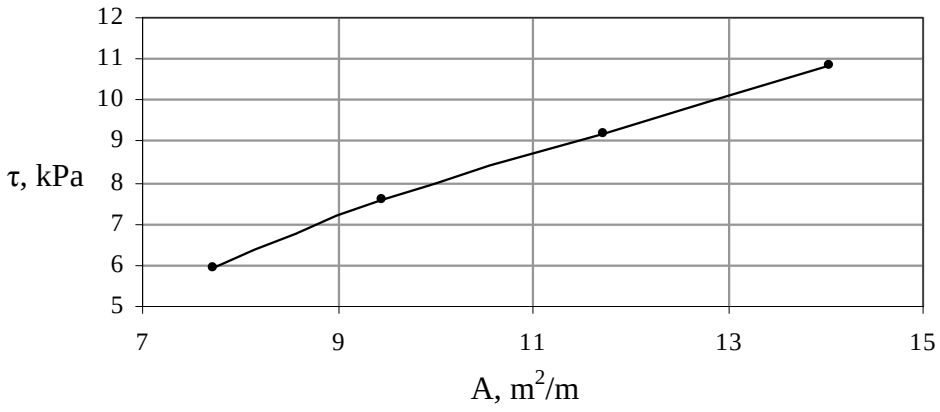

Fig. 5. Shear strength versus contact area, σ = 5 kPa, φ = 30º

Table 2. Typical values of contacts between ice blocks as given by the block generator

Total contact area A, m^2/m	Average length $\bar{l}$, m
7.57	0.122 ± 0.085
9.31	0.150 ± 0.087
12.15	0.196 ± 0.092
14.74	0.238 ± 0.120

Additionally it was found that the total amount of blocks N and the inclination angles of contacts θ are very important as well. For the present simulation series the total amount of contacts was in narrow range of 60-62. It was also observed that θ is one of the contributors, which determined the failure mechanisms between the ice blocks and therefore has influence on the shear strength.

Influence of normal pressure

For the range of the present analysis shear strength τ increased non-linearly with increase of normal pressure σ as shown in Fig. 6.

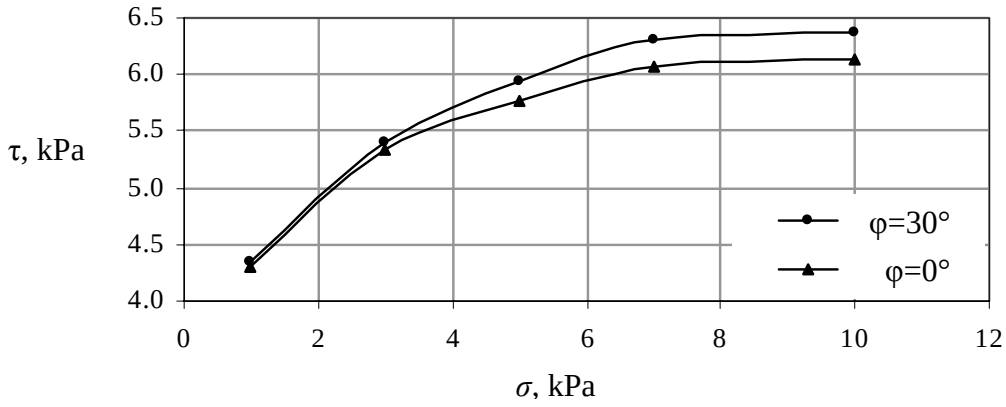

Fig. 6. Shear strength versus normal pressure

The analysis shows that strength of the ice rubble is largely determined by the tensile strength. The stress states inside the ice rubble are illustrated in Fig 7. The plastic Mohr-Coulomb stress points are indicated with white dots and the tension cut-off points are indicated with black dots. For normal pressure σ = 1 kPa the ice rubble fails mostly in tension (Fig. 7a). The failure mode changes with increasing normal pressure up to 5 kPa. The local failure mechanism becomes a combination of tension and shear modes (Fig. 7b). It is possible to see from the Fig. 6 that shear strength increases approximately linearly with increasing of normal pressure up to 5 kPa. The failure mechanism remains the same with further increasing of normal pressure (Fig. 7c). Therefore the curves become non-linear and more flat as shown in Fig. 6.

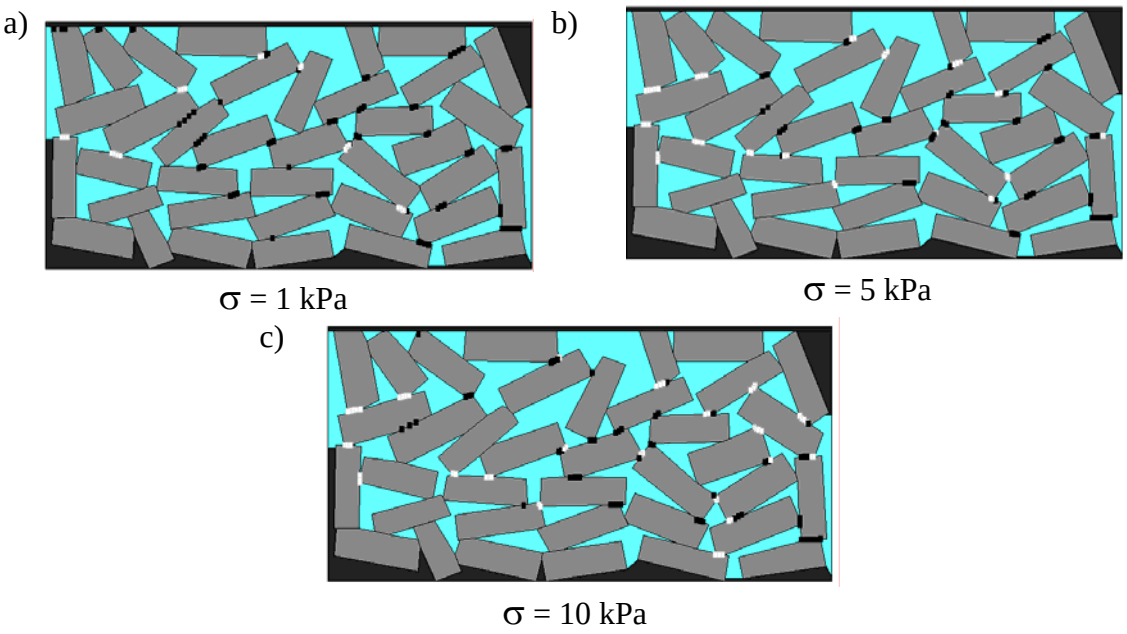

Fig. 7. Stress state inside the ice rubble $R_i = 0.09$, $\varphi = 30^o$
(White dots - Coulomb stress points, black dots - tension cut-off points)

CONCLUSIONS

The paper presents pseudo-discrete continuum model that simulates the breakage of rubble skeleton. A series of direct shear-box tests are done. The simulations were performed in order to investigate the effect mechanical properties of the ice blocks and their contacts. The influence of normal pressure on the ice rubble strength was analyzed.

The parametric analysis showed the following:

- The failure of the ice rubble mostly occurs between the ice blocks. But some local breakage of individual ice blocks was also observed during simulations. The initial failure mode is independent of frictional component. Therefore cohesion is a major contributor to the bearing capacity of the ice rubble.

- The freeze-bond properties and their relations to the properties of parent ice are important. The shear strength linearly increases with increasing strength of the interface elements.

- The shear strength of the freeze-bond linearly increases with increasing of contact area. Contact area between ice blocks, amount of contacts and inclination angles of contacts has a great influence on failure mode and shear strength. Thus it seems to be of high importance to estimate these parameters in-situ.

- The shear strength increased non-linearly with increasing of normal pressure. Strength of the ice rubble is mostly determined by tensile strength. But the some changes of failures mechanisms from tension to shear modes were observed, which probably is the result to the non-linear behaviour.

ACKNOWLEDGEMENTS

The authors would like to thank Alexey Privalov and Lev Videnski for programming support. We would also like to thank Dr. Knut Høyland for extensive review and valuable comments.

REFERENCES

Bruneau, S., 1997. Development of a first-year ridge load model. *PhD thesis, Memorial University of Newfoundland*, St. John's, Newfoundland, Canada (1997).

Ettema, R. and Schaefer, J.A. Experiments on freeze-bonding between ice blocks in floating ice rubble. *Journal of Glaciology*, Vol. 32, No. 112: 397-403 (1986).

Ettema, R. and Urroz, G.E. On internal friction and cohesion in unconsolidated ice rubble. *Cold Regions Science and Technology*, 16: 237–247 (1989).

Ettema, R. and Urroz, G.E. Friction and cohesion in ice rubble reviewed. *Proc. of the 6th Int. Speciality Conf. Cold Regions Engineering*. Hanover, USA (1991) 316-325.

Heinonen, J. Continuum material model with shear-cap yield function for ice rubble. *Proc. of 15th Nordic Seminar on Computational Mechanics*. Aalborg, Denmark (2002) 87-90.

Heinonen, J. Continuum material model for ice rubble – combined shear-cap yield criterion with strain softening. *Proc. of the 17th Int. Conf. on Port and Ocean Engineering under Arctic conditions.* Trondheim, Norway (2003) 547–557.

Hopkins, M.A. and Hibler, W.D. On the shear strength of geophysical scale ice rubble. *Cold Regions Science and Technology*, 19: 201-212 (1991).

Kämärinen, J. Studies in ice mechanics. *Helsinki University of Technology.* Finland (1993) 182 p.

Liferov, P., Jensen, A., Høyland, K.V. and Løset, S. On analysis of punch tests on ice rubble. *Proc. of the 16th Int. Symp. on Ice.* Dunedin, New-Zealand (2002) 101–109.

Liferov, P., Jensen, A. and Høyland, K.V. 3D finite element analysis of laboratory punch tests on ice rubble. *Proc. of the 17th Int. Conf. on Port and Ocean Engineering under Arctic conditions.* Trondheim, Norway (2003) 599–610.

PLAXIS Plaxis v. 8.1. Finite Element Code for Soil and Rock Analyses (2002).

Timco, G.W. and Cornet, A.M., 1999. Is φ a constant for broken ice rubble? *Proc. of the 10th Workshop on River Ice Management with a Changing Climate*. Winnipeg, Manitoba, Canada (1999) 318–331.

Weiss, R.T., Prodanovic, A. and Wood, K.N. Determination of ice rubble shear properties. *Proc. of the Int. Symp. on Ice.* Quebec, Canada, (1981) 860-872.

17th International Symposium on Ice
Saint Petersburg, Russia, 21-25 June 2004
International Association of Hydraulic Engineering and Research

ICE DYNAMIC MODEL WITH A VISCOELASTIC-PLASTIC CONSTITUTIVE LAW

Shunying Ji [1,2], Hung Tao Shen [2], Zhilian Wang [2], Hayley Shen [2], and Qianjin Yue [1]

ABSTRACT

In this study, a viscoelastic-plastic (VEP) constitutive model for ice dynamics is developed. This model consists of a Kelvin-Vogit model for viscoelastic behavior, the Mohr-Coulomb yielding criterion, and the associated normal flow rule for plastic rheology. In the Mohr-Coulomb yielding criterion, the hydrostatic pressure determines the ice strengths under convergent and divergent conditions. Numerical simulations of ice motion in an idealized rectangular basin, and ice dynamics of Bohai Sea were carried out using Smoothed Particle Hydrodynamics (SPH) method.

INTRODUCTION

The internal ice force described by a constitutive model is the most complex term in the equation of motion of sea ice dynamics. It is also an important term affecting the results of sea ice simulation. The existing constitutive models for sea ice dynamics include viscous plastic (VP) model (Hibler, 1979), elastic plastic (EP) model (Coon et al. 1974, Pritchard 1975), viscous elastic plastic model coupled with granular flow dynamics (Shen et al. 1987, Hopkins 1996), and anisotropic models (Hibler 2001, Coon et al. 1998, Pritchard 1998). In this paper, a viscoelastic-plastic (VEP) model for sea ice dynamics is developed, in which the ice cover is assumed to be viscous-elastic under small strain and strain rate, and a plastic rheology is assumed under large strain rate, where a Mohr-Coulomb yielding criterion is considered. Like the existing VP and VE models, this VEP model is also based on the assumption of a two-dimensional isotropic continuum medium. The present VEP model is implemented in the SPH ice dynamics model (Shen et al. 2000, Wang et al. 1999) to simulate ice motion in a rectangular basin and in the Bohai Sea.

1 Department of Civil and Environ. Engrg., Clarkson University, Potsdam, New York 13699-5710, USA. Email: jisy@clarkson.edu or htshen@clarkson.edu
2 State Key Laboratory of Structural Analysis for Industrial Equipment, Dalian University of Technology, Dalian 116023, China.

VISCO-ELASTIC PLASTIC MODEL

In the present model, we use Kelvin-Vogit model to describe the visoelastic behavior of the sea ice. Coupling with the plastic rheology, the viscoelastic-plastic model is established as shown in Fig.1. The spring, dashpot, and sliding block represent the elastic, viscous and plastic properties, respectively.

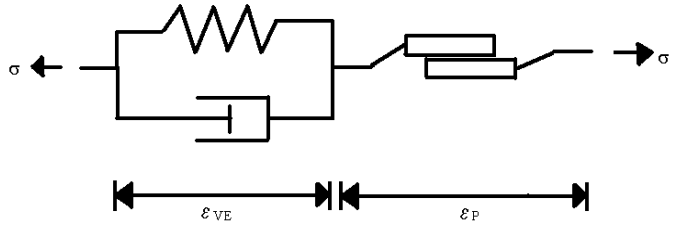

Fig. 1. Viscoelastic-plastic model for sea ice dynamics

The stress-strain relationship of a viscoelastic model can be written as

$$\sigma_{ij} = 2\eta_V \dot{\varepsilon}_{ij} + (\zeta_V - \eta_V)\dot{\varepsilon}_{kk}\delta_{ij} + 2G\varepsilon_{ij} + (K - G)\varepsilon_{kk}\delta_{ij} - P_r\delta_{ij}\,, \tag{1}$$

where, ζ_v and η_v are the bulk and shear viscosities; P_r is the hydrostatic pressure; and K and G are the elastic bulk and shear modulus respectively:

$$K = \frac{E}{2(1-\upsilon)} \quad \text{and} \quad G = \frac{E}{2(1+\upsilon)}\,. \tag{2}$$

In the above, E is the Young's modulus, and υ is the Poisson's ratio. The elastic modulus of ice cover can be formulated as a function of ice concentration, $E = E_0\left(\frac{N}{N_{\max}}\right)^j$, in which $j = 15$ is an empirical constant, N is the ice concentration, and N_{max} is its maximum possible ice concentration. The ice viscosities may be expressed in a similar form.

The Mohr-Coulomb friction law has been introduced into ice dynamics (Shen et al. 1990). In terms of principle stresses σ_1 and σ_2, the yield criterion can be written as

$$f(\sigma_1,\sigma_2) = \sigma_1 - \sigma_2 + (\sigma_1 + \sigma_2)\sin\varphi - 2c\cos\varphi = 0, \tag{3}$$

where, c is the cohesion, and φ is the friction angle. The Mohr-Coulomb yield surface is a hexagonal cone in 3-D principle stress space, as shown in Fig. 2. When the hydrostatic pressure is nonzero, the principle stress in the z-direction is $\sigma_3 = -P_0$. This yield function is determined by three parameters: frictional angle, cohesion, and hydrostatic pressure.

The Mohr-Coulomb yielding condition is defined by three distinct surfaces, i.e. the shear, convergent, and divergent surfaces, which can be written as

$$\sigma_1 = K_D\sigma_2 + 2c\sqrt{K_D}\,, \tag{5}$$

$$\sigma_C = -K_C P_0 - 2c\sqrt{K_C}\,, \tag{6}$$

$$\sigma_T = -K_D P_0 + 2c\sqrt{K_D}\,, \tag{7}$$

with $K_D = \tan^2\left(\frac{\pi}{4} - \frac{\varphi}{2}\right)$, and $K_C = \tan^2\left(\frac{\pi}{4} + \frac{\varphi}{2}\right)$.

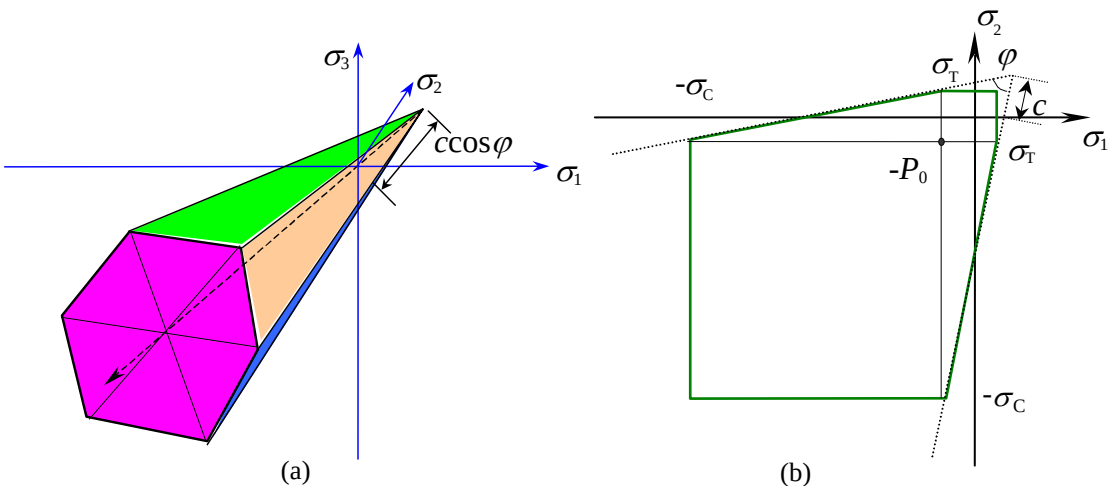

Fig. 2. Mohr-Coulomb yielding criterion in 3D and 2D

When ice enters the plastic state under large deformation, the principle stress falls on the yield surface. The deformation includes two components: elastic and plastic strains

$$d\varepsilon_{ij} = d\varepsilon_{ij}^{\mathrm{e}} + d\varepsilon_{ij}^{\mathrm{p}}, \tag{8}$$

where $d\varepsilon_{ij}^{\mathrm{e}}$ and $d\varepsilon_{ij}^{\mathrm{p}}$ are the increments of elastic and plastic strains. The elastic stress increment can be expressed as

$$d\sigma_{ij} = \mathbf{D}^{\mathrm{el}}(d\varepsilon_{ij} - d\varepsilon_{ij}^{\mathrm{p}}), \tag{9}$$

where $\mathbf{D}^{\mathrm{el}}$ is the elastic modulus tensor. When the material is in the elastic state, we have $d\varepsilon_{ij}^{\ \mathrm{p}} = 0$. When it is in plastic state, strain can be determined with the normal associated flow rule. The Mohr-Coulomb yielding function is used as the plastic potential function, and the direction of plastic strain rate is normal to the yielding curve. According to Drucker's theory, we may express the normality rule as

$$d\varepsilon_{ij}^{\mathrm{p}} = d\lambda \frac{\partial \Psi}{\partial \sigma_{ij}}, \tag{10}$$

where $d\lambda$ is the plastic multiplier, and Ψ is the plastic potential function, which is set as the yield curve $f(\sigma_{ij})$ in this paper.

In a floating ice field, the mean vertical hydrostatic pressure can be written as (Shen et al. 1990)

$$P_0 = \left(1 - \frac{\rho_{\mathrm{i}}}{\rho_{\mathrm{w}}}\right) \frac{\rho_{\mathrm{i}} g t_{\mathrm{i}}}{2} \left(\frac{N}{N_{\max}}\right)^j \tag{11}$$

where, P_0 is the mean pressure in vertical direction, and ρ_{i} and ρ_{w} are densities of ice and water. The horizontal hydrostatic pressure can be calculated as $P_{\mathrm{r}} = K_0 P_0$, in which P_{r} is the horizontal hydrostatic pressure, and $K_0 = 1 - \sin\varphi$.

NUMERICAL SIMULATIONS

Analytical and numerical solutions of ice ridging in a rectangular basin - The steady state profile of ice ridge, formed by unidirectional wind and water drag in a rectangular basin initially covered by uniform ice thickness and concentration, can be derived analytically. Using traditional VP model, modified VP model, classical jamming theory, and VEP model, the steady state ice ridging thickness profiles are plotted in Fig. 3. Model parameters are listed in Table 1. The ice ridging process in the regular basin with bank friction can be simulated with VEP model. The mean thickness and distribution of stresses are plotted in Figures 4 and 5.

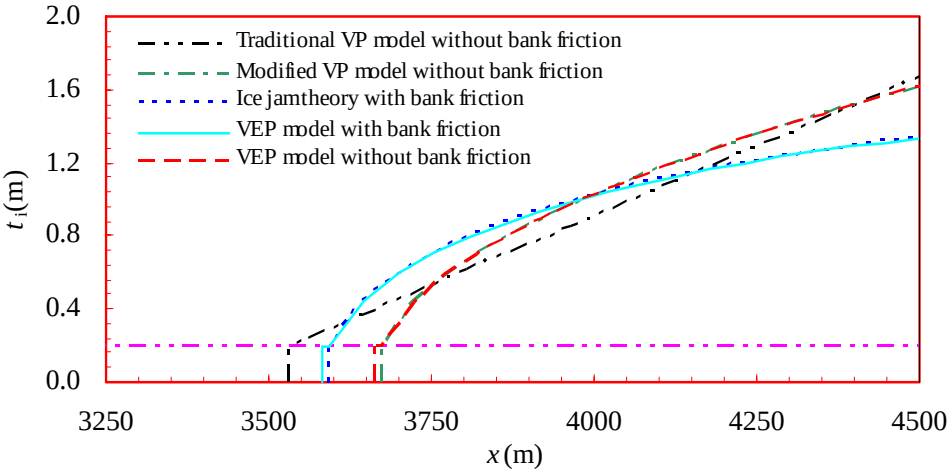

Fig. 3. Analytical solutions of ice thickness profile with different constitutive models

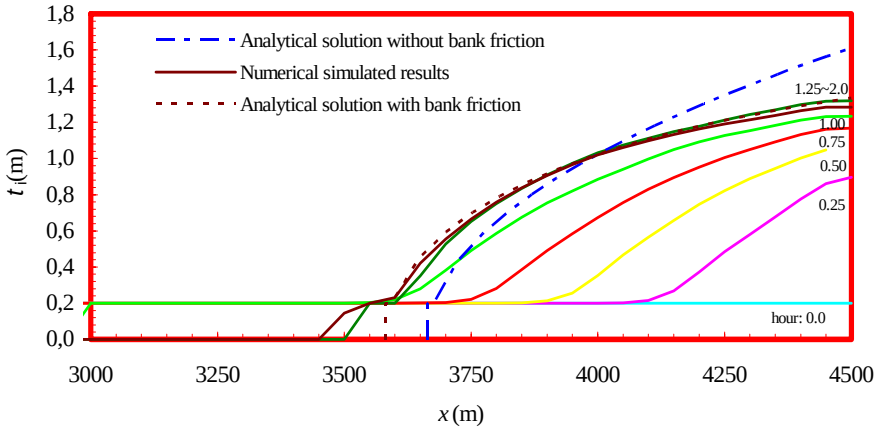

Fig.4. Ice ridging thickness simulated from VEP model and analytical solutions

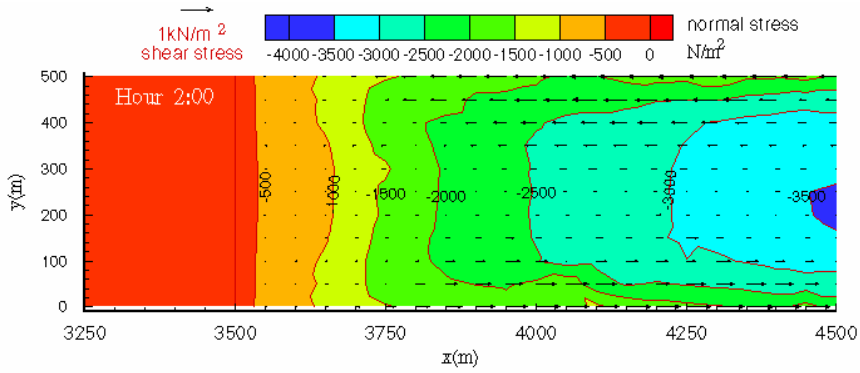

Fig. 5. Distributions of shear and normal stresses in x direction

Simulation of Bohai Sea ice dynamics – The dynamics of Bohai Sea ice is simulated with the VEP model, and compared the simulations using traditional VP model (Hibler 1979) and modified VP model (Shen et al. 1990). The initial ice thickness and concentration are estimated from the NOAA satellite remote images. The input wind field is determined with an operational atmospheric model (Wang 2000). The tidal current is simulated with two-dimensional shallow water equations solved by an ADI finite difference method (Zhang 2000). The main model parameters are the same as listed in Table 1. Additional parameters used in the simulations are listed in Table 2. The simulated ice conditions at the JZ20-2 oil/gas platform in Liaodong Bay are presented. From these three models the ice velocities are almost the same, because ice drift is dominated by the tidal current. The divergences of ice velocity simulated with VEP model and modified VP model vary with the tidal cycle, while that of traditional VP model has a strong random fluctuation (Figure 6). The same phenomenon appears in the stresses. The stress magnitudes simulated with VEP model and modified VP model are very close, and they are much lower than that of the traditional VP model (Figure 7). If we reduce the pressure P^* of the traditional VP model from 5.0×10^3 to 1.0×10^3 N/m^2, the fluctuation of ice stress and velocity divergence can be reduced. From the principal stress of the three models it can be seen that the ice cover appears to be in the plastic regime (Figure 8).

Table 1. Parameters used in the ice ridging simulation

Variable	Definition	Value	Variable	Definition	Value
t_{i0}	Initial ice thickness	0.2 m	N_0	Initial ice concentration	100%
B	Width of ice field	500 m	L	Initial ice length	4500 m
φ	Ice frictional angle	46°	P^*	Ice strength in traditional VP model	1.0×10^4 N/m^2
v	Possion's ratio	0.3	ζ_{v0}	Bulk viscosity	1.0×10^6 N·s/m^2
V_a	Wind speed	15.0 m/s	η_{v0}	Shear viscosity	2.5×10^5 N·s/m^2
V_w	Current speed	0.4 m/s	E_0	Young's modulus	1.0×10^5 N/m^2
c_a	Wind drag coefficient	0.015	c_w	Current drag coefficient	0.02
Δt	Time step	0.5 s	ΔS	Initial parcel size	50 m

Table 2. Additional parameters used in the sea ice dynamics simulation of Bohai Sea

Variable	Definition	Value	Variable	Definition	Value
c_a	Wind drag coefficient	0.0015	ζ_{max}	Maximum bulk viscosity	1.0×10^{10} N·s/m^2
c_w	Current drag coefficient	0.0025	Δt	Time step	40s
P^*	Ice strength of VP model	5000 N/m^2	ΔS	Initial ice parcel dimension	2km

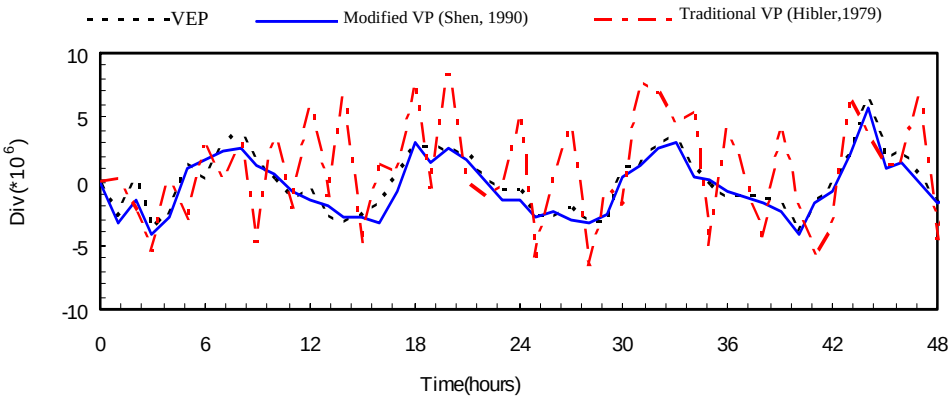

Fig. 6. Velocity divergence simulated in 48 hours at the JZ20-2 area

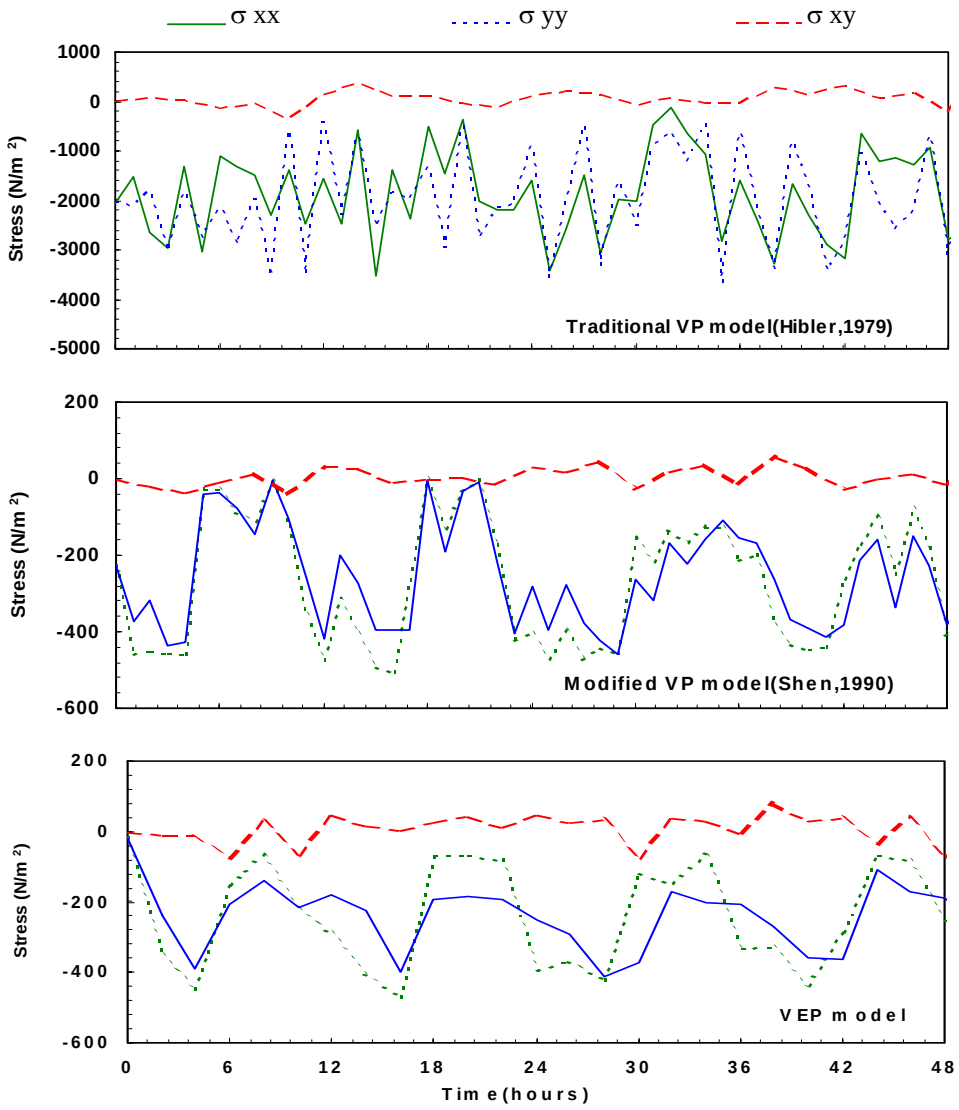

Fig. 7. Sea ice stresses simulated in 48 hours at the JZ20-2 area

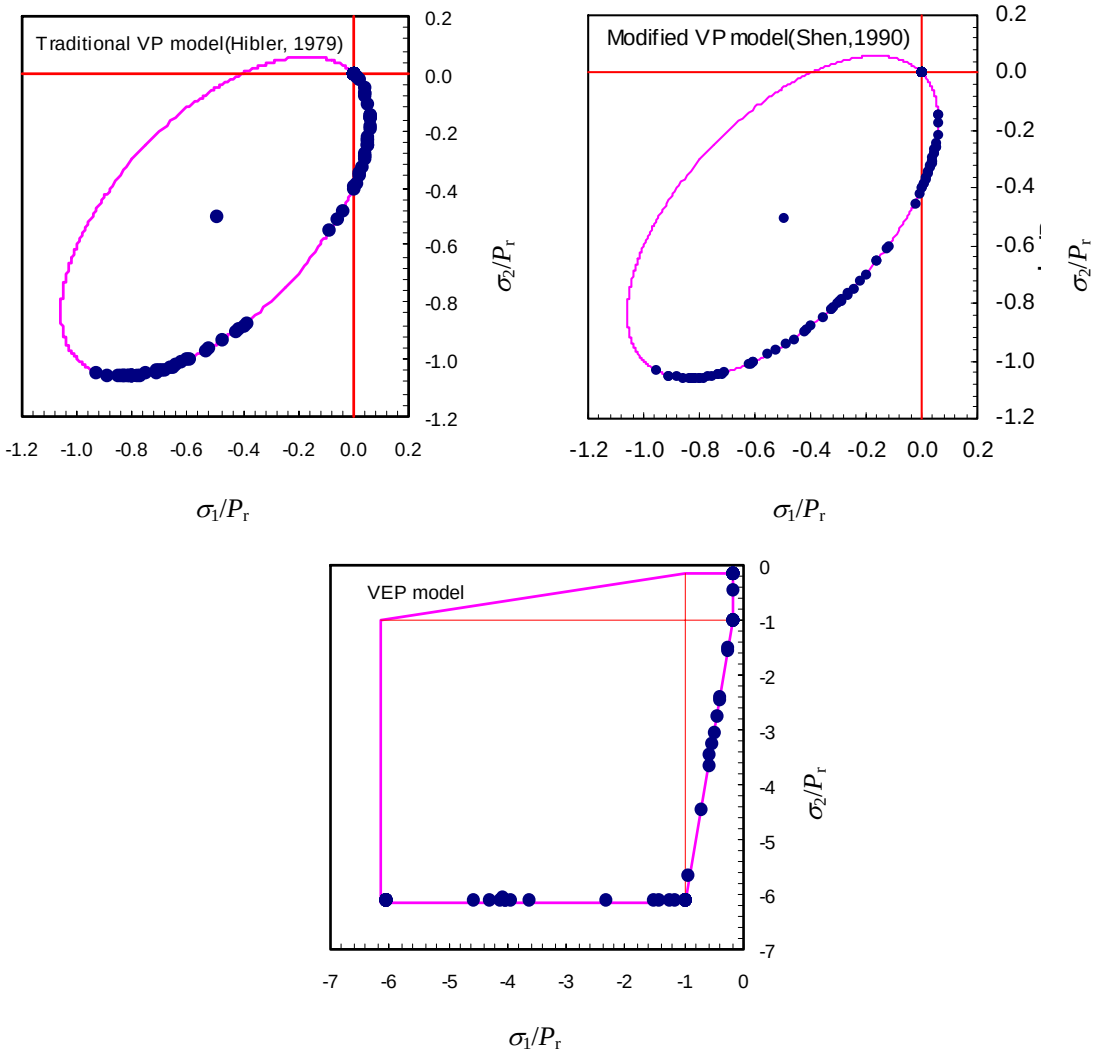

Fig. 8. Principal stress state of sea ice simulated at the JZ20-2 area

CONCLUSIONS

A viscoelastic-plastic (VEP) constitutive model for ice dynamics is presented along with numerical simulations. In this VEP model, ice cover under both the viscous-elastic behavior before yielding, and the plastic rehology after yielding are considered. The Mohr-Coulomb yielding criterion, the associated normal plastic flow rule, and the hydrostatic ice pressure are used. With this VEP model, the ice ridging process in rectangle basin is simulated and compared with the analytical solution. The ice dynamic process in the Bohai Sea is simulated and compared with the traditional VP model, and the modified VP model. From these comparisons, it is found that the present VEP model can simulate the ice edge and ice thickness distribution more accurately. The stability of the VEP model is also verified with the simulated ice parameters at the JZ20-2 area.

REFERENCES

Coon, M.D., Knoke, G.S., Echert, D.C. and Pritchard, R. The architecture of an anisotropic ealsitc-plastic sea ice mechanics constitutive law. *Journal of Geophysical Research*, 103(C10): 21915-21925 (1998).

Coon, M.D., Maykut, S.A., Pritchard, R.S., Rothrock, D.A., and Thorndike, A.S. Modeling the Pack Ice as an Elastic Plastic Material. *AIDJEX Bull*., 24: 1-105 (1974).

Hibler, W.D. A Dynamic Thermodynamic Sea Ice Model. *Journal of Geophysical Oceanography*, 9: 817-846 (1979).

Hibler, W.D. Sea ice fracturing on the large scale. *Engineering Fracture Mechanics*, 68: 2013-2043 (2001).

Hopkins, M.A. On the mesosacle interaction of lead ice and floes. *Journal of Geophysical Research*, 101(C8): 18315-18326 (1996).

Pritchard, R.S. An Elastic-Plastic Constitutive Law for Sea Ice. *Journal of Applied Mechanics*, 42: 379-384 (1975).

Pritchard, R.S. Ice conditions in an anisotropic sea ice dynamics model. *International Journal of Offshore and Ploar Engineering*, 8:9-15 (1998).

Shen, H.H., Hibler W.D. and Lepparanta, M. The role of floe collisions in sea ice rheology. *Journal of Geophysical Research*, 94(C10): 14525-14537 (1987).

Shen, H.T., Shen, H.H. and Tsai, S.M. Dynamic transport of river ice. *Journal of Hydraulic Research*, 28(6):659-671 (1990).

Shen, H.T., Su, J. and Liu, L.W. SPH simulation of river ice dynamics. *Journal of Computational Physics*, 165:752-770 (2000).

Wang, Z.L. A Coastal Sea Ice Model with Discrete Parcel Method. *CEE Report* 99-16, Clarkson University, Potsdam, NY, 146 (1999).

Zhang Z. H. On modeling ice dynamics of semi-enclosed seasonally ice-covered seas. *Report Series in Geophysics*. University of Helsinki, (2000).

17th International Symposium on Ice
Saint Petersburg, Russia, 21-25 June 2004
International Association of Hydraulic Engineering and Research

THERMODYNAMIC CONSOLIDATION OF SEA ICE RIDGES

Aleksey Marchenko[1], Alexandr Makshtas[1, 2], Yurii Gudoshnikov[1] and Gennagii Zubakin[1]

ABSTRACT

A model of thermodynamic consolidation of sea ice ridges is considered. Temperature and porosity distributions inside the ridge are calculated for self-similar problem about the consolidation of homogeneous rubble ice and for realistic floating ridge.

INTRODUCTION

The ice ridge is formed during several tens minutes. During this time sufficiently large number of cold ice blocks, which surface temperature is closed to atmosphere temperature, become submerged in sea water with temperature about -2C. Although initially ice ridge consists from unfrozen ice blocks, which can displace relatively each other, the influence of atmosphere cooling causes the formation of consolidated layer (CL) in the middle part of the ridge. The thickness of CL can be several times greater the thickness of level ice which was formed under the same meteorological conditions. For example, the CL of ridges can reach 8 m in Pechora sea. Field studies of internal structure of ice ridges are based on vertical drilling of the ridges in several points. The porosity of the ice on different levels of the ridge in each drilling location is estimated by vertical speed of the drill. Vertical structure of the ridge is studied in several vertical holes, and then these data are extrapolated to renew 3D structure of the ridge and to estimate its strength. The studies show that there are unfrozen regions inside ridges filled by shuga (mixture of ice crystals and brine) and sea water.

Hoyland (2002) elaborated FEM model of thermodynamic consolidation of floating ice ridge based on the law of internal energy balance taking into account volume crystallization of sea water below the consolidated layer of the ridge. He found that the ratio of consolidated layer thickness to level ice thickness is changed from 1.6 to 2. Marchenko et al., (2003a, 2003b) considered self-similar problems about the consolidation of homogeneous rubble ice taking into account salt diffusion and volume crystallization processes. They found the same estimations for the thickness of consolidated layer as Hoyland (2002) and the increasing atmosphere-ocean heat fluxes in the initial period of the consolidation. In the present work we formulated more realistic model of the consolidation and improve estimations of the CL thickness, temperature and porosity distributions inside the ridge.

[1] Arctic and Antarctic Research Institute, Beringa str. 38, 199397 St.Petersbutg, Russia
[2] · International Arctic Research Center, University of Alaska, Fairbanks, USA

BASIC EQUATIONS

A ridge is considered as a mixture of solid ice blocks, ice crystals and sea water between them. It is assumed that temperature T of these components is equal to the temperature of salt water freezing $T_f = -\Gamma S$, where S is water salinity and $\Gamma \approx 56.6^\circ$C/ppt . Fractional volume of the water inside the ridge is characterized by porosity $\nu \in (0,1)$. Heat conductivity equation is written as follows

$$\left(\rho_w c_{v,w}\nu + \rho_i c_{v,i}(1-\nu)\right)\frac{\partial T}{\partial t} + Q\frac{\partial \nu}{\partial t} = \nabla\left[(C_w\nu + C_i(1-\nu))\nabla T\right], \qquad (1)$$

where T is temperature, ρ_w and ρ_i are water and ice densities, $c_{v,i}$ and $c_{v,w}$ are the specific heat capacity of ice and water, Q is the latent heat, C_i and C_w are the thermal conductivities of ice and water, t is the time, $\nabla = (\partial/\partial x, \partial/\partial y, \partial/\partial z)$ is differential operator, x, y and z are horizontal and vertical coordinates. Salt diffusion in the water is described by equation

$$\frac{\partial(\nu S)}{\partial t} = D\nabla\cdot\left(\nu\nabla S\right), \qquad (2)$$

where S is water salinity and D is coefficient of salt diffusion. Equations (1) and (2) together with condition $T = T_f$ are used for the finding of T, S and ν. We distinguish solid ice fraction with $\nu < 0.2$, where $D = 0$, and the mixture of sea water with ice crystals with $\nu > 0.2$, where $D > 0$ is the coefficient of molecular diffusion.

Table 1. Numerical values of ice and water characteristics

ρ_w	ρ_i	$c_{v,i}$	$c_{v,w}$	C_i	C_w	Q	D
1020 kg/m^3	910 kg/m^3	2.09 kJ/kg K	4.19 kJ/kg K	2.24 W/m K	0.58 W/m K	3.34 10^5 kJ/m^3	1.45 10^{-9} m^2/s

CONSOLIDATION OF RUBBLE ICE, SELF-SIMILAR PROBLEM

It is assumed that in initial time $t = 0$ half-space $z > 0$ is filled by rubble ice with initial porosity $\nu_r > 0.2$. Initial temperature of the rubble is $T_r = -1.98^\circ$C, while the temperature of boundary $z = 0$ is $T_a < T_r$. The cooling causes the formation of solid ice called as consolidated layer (CL) in the vicinity of boundary $z = 0$. At the boundary between solid ice and the rubble we set the continuity of the temperature and consider boundary conditions for the heat and salt fluxes:

$$Q(\nu_+ - \nu_i)\frac{dh}{dt} = \lim_{z\to h-0}\left(C_w\nu_i + C_i(1-\nu_i)\right)\frac{\partial T}{\partial z} - \lim_{z\to h+0}\left(C_w\nu_+ + C_i(1-\nu_+)\right)\frac{\partial T}{\partial z}, \qquad (3)$$

$$(S_+\nu_+ - S_i\nu_i)\frac{dh}{dt} = -D\nu_+\lim_{z\to h+0}\frac{\partial S}{\partial z},\ \lim_{z\to h-0} T = \lim_{z\to h+0} T\,.$$

Here h is the CL thickness, $\nu_i = 0.2$ is solid ice porosity at the lower boundary of the CL, ν_+ is unknown porosity of the rubble below the CL. Inside the CL equations (1) and (2) with $D = 0$ are used, below the consolidated layer $D > 0$.

Self-similar solution of equations (1) and (2) depends on dimensionless variable $\varsigma = z/(l_*\sqrt{t/t_*})$, and thickness of the consolidated layer is $h = Al_*\sqrt{t/t_*}$, where con-

stant A is defined from the solution, l_* is representative length scale and $t_* = l_*^2 \rho_i c_{v,i} / C_i$. From Tab. 1 we find that $t_* \approx 10$ days when $l_* \approx$ 1 м. Example of self-similar solution is shown on Fig. 1a,b for the case $T_a = -20^\circ\mathrm{C}$ and $\nu_r = 0.3$. Fig. 1c shows the dependence of constant A from temperature T_a for $\nu_r = 0.3$ and $\nu_r = 0.4$ by dots. From Fig. 1c follows that $A \approx 0.87$ when $T_a = -20^\circ\mathrm{C}$ and $\nu_r = 0.3$. From Fig. 1a follows almost linear temperature profile within the CL. Fig. 1b shows the existence of thin boundary layer below the CL where the porosity is changed from 0.2 to 0.3. Continuous line at Fig 1c shows the thickness of level ice floating on the surface of sea water calculated from self-similar problem, where salinity and temperature below the ice are given constants. One can see that the ratio of the CL layer thickness to the level ice thickness is changed from 1.5 to 2 depending on the surface temperature T_a. It has a good agreement with simulations of Hoyland (2002).

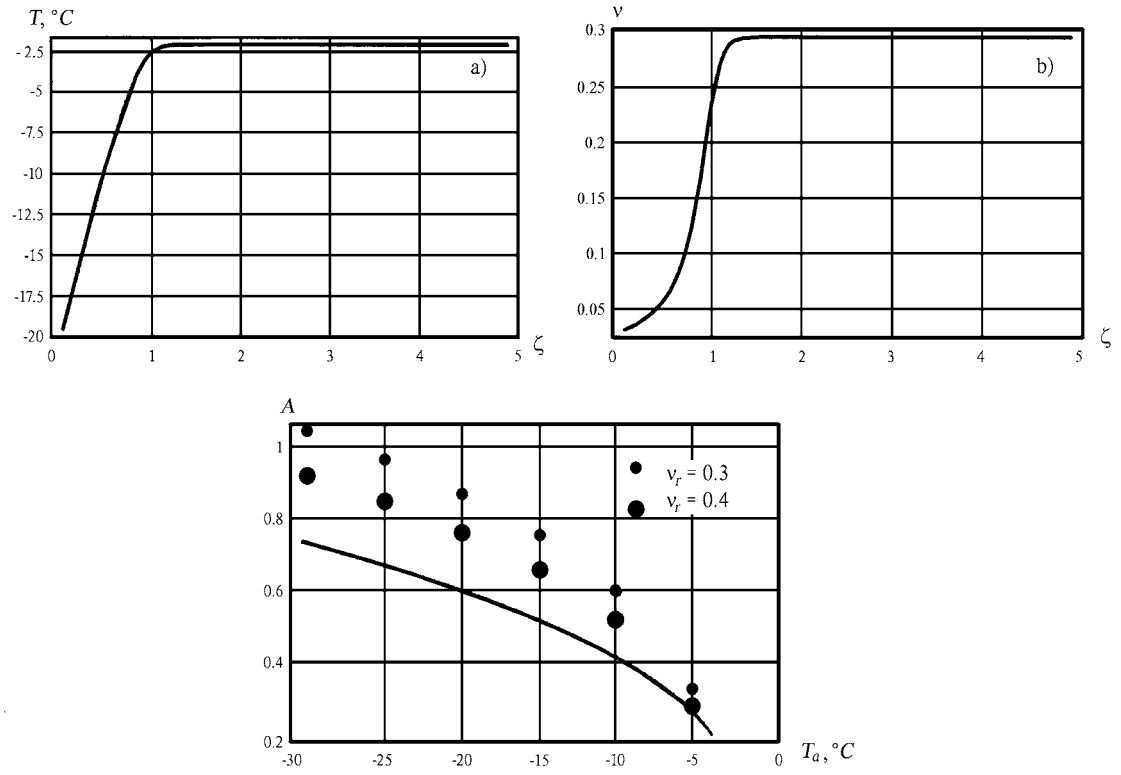

Fig. 1. Example of the dependencies of the temperature (a) and porosity (b) from self-similar variable ζ for T_a = –20°Cand ν_r = 0.3. Constant A versus temperature T_a for the values of rubble ice porosity ν_r = 0.3 and ν_r = 0.4, continuous line is related to open water freezing (ν_r = 1) (c)

CONSOLIDATION OF REALISTIC FLOATING RIDGE.

Time-dependent model of ice ridge consolidation is elaborated to describe the evolution of ridge porosity ν and temperature T under given meteorological conditions in the cold time of a year. Energy is transferred between the ridge and its surroundings; the ocean beneath and the air above. It is assumed that water temperature below the ridge is closed to the temperature of sea water freezing ~ -2^o C. Energy is taken away through the top surface, and the energy exchange with the surrounding air consists of turbulent

fluxes (sensible (*H*) and latent (*LE*)) and radiation balance (*R*). Radiation is treated as a surface flux in the model. Thus boundary condition on the top surface of the ridge is formulated as follows

$$-C_i \frac{\partial T}{\partial n} = H + LE + R, \tag{4}$$

where $\partial T / \partial n$ denotes normal derivative from the temperature. Fluxes *H*, *LE* and *R* are calculated by the use of the air temperature, the wind speed, the specific heat capacity of air, the relative humidity of the air, the density of air, the albedo and the surface temperature. The formulas for the fluxes are taken from Makshtas (1991).

Initial porosities of solid ice, shuga and water are 0.05, 0.5-0.6 and 1 respectively. They are denoted as black, gray and white regions at Fig.2. Initial temperature of sea water and shuga between ice blocks is –2°C. Air temperature and wind velocity are –20°C and 10 m/s respectively.

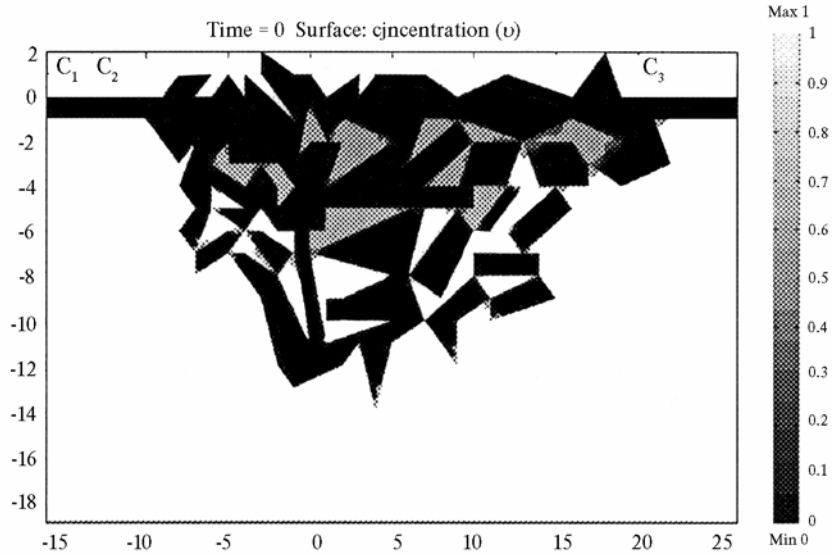

Fig. 2. Solid ice blocks composed the ridge is shown by black color,
gray regions show shuga between ice blocks, white regions show sea water

Figures 3 show the results of numerical simulations with initial temperature of solid ice blocks T_0 = –11°C (a,b) and T_0 = –3°C (c,d) for two months consolidation. Figure 3a shows the existence of the consolidated ice, which porosity is changed from 0.05 inside solid ice blocks to 0.4 between them, in the central part of the ridge up to 7 m depth when T_0 = –11°C. The thickness of level ice remains during this time smaller 2 m. Figure 3c shows that lower boundary of the consolidated ice in the central part of the ridge is located on 2.5 m depth when T_0 = –3°C.

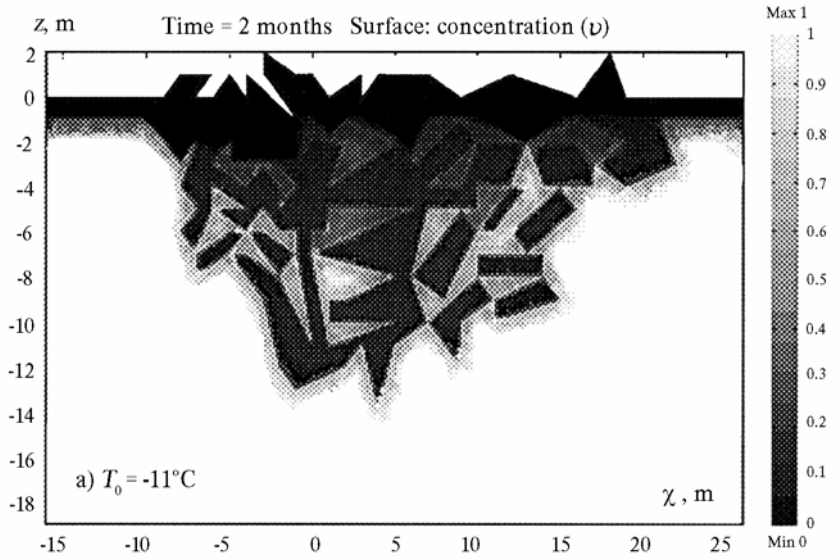
z, m
Time = 2 months Surface: concentration (υ)
Max 1
Min 0
a) T_0 = -11°C
χ , m

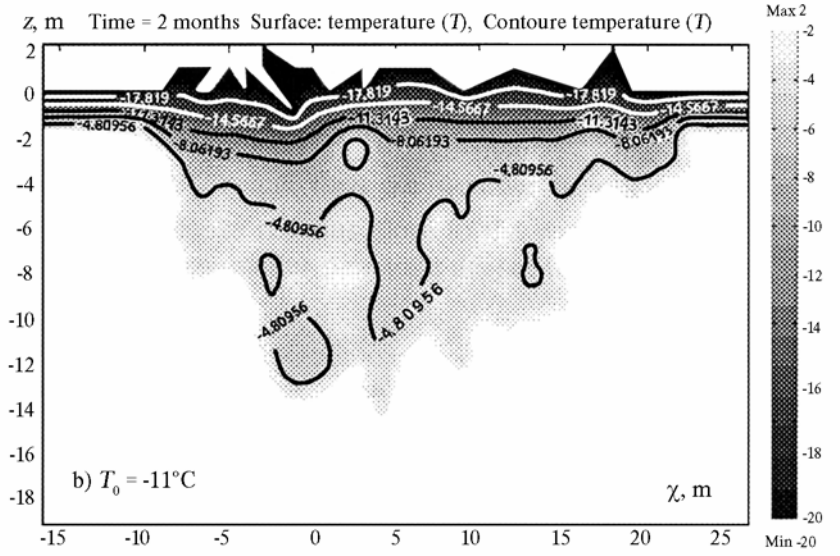
z, m
Time = 2 months Surface: temperature (T), Contoure temperature (T)
Max 2
Min -20
-17.819
-14.5667
-11.3143
-8.06193
-4.80956
b) T_0 = -11°C
χ, m

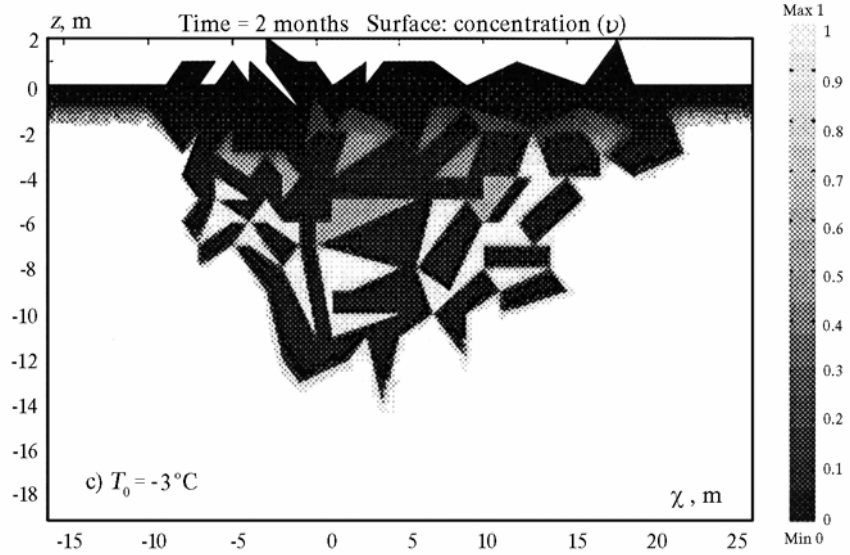
z, m
Time = 2 months Surface: concentration (υ)
Max 1
Min 0
c) T_0 = -3°C
χ , m

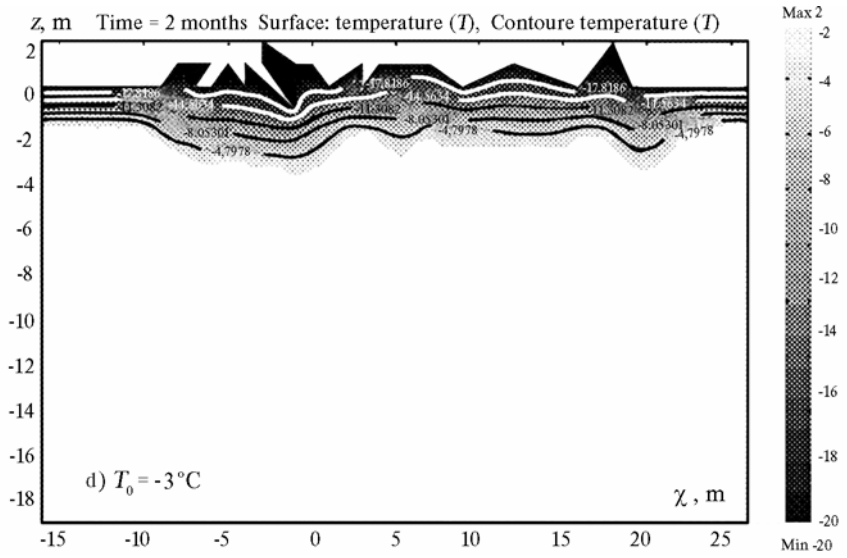

Fig. 3. The distribution of the porosity (a,c) and the temperature (b,d) after two months consolidation. Initial values of solid ice temperature T_0 are shown at the figures

Figure 3b shows that low temperature anomalies up to –5°C are conserved inside solid ice blocks during two months when T_0 = –11°C. When the ridging is occurred in the warm weather (T_0 = –3°C), and then the weather becomes cold, the temperature of deeply submerged ice blocks remains close to the water temperature (Fig. 3d). Nevertheless low temperature anomalies penetrate deeper in the middle part of the ridge than below the level ice.

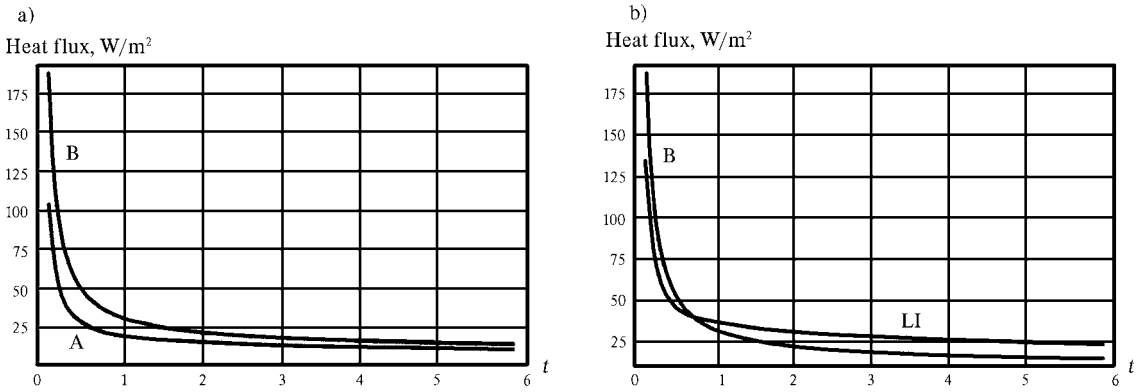

Fig. 4. Heat fluxes averaged over the surface of ridged ice (lines A and B) and heat flux over the surface of level ice (line LI) versus the time

Lines A and B on Fig. 4 show the heat fluxes averaged over the surface of ridged ice (segment C_2C_3 on Fig. 2), and line LI shows the heat flux averaged over the surface of level ice (segment C_1C_2 on Fig. 2). Line A is constructed when T_0 = –11°C, and lines B and LI are constructed when T_0 = –3°C. One can see that the heat flux through the ridged ice is larger the heat flux through 1m level ice during the first week of the consolidation.

DISCUSSIONS AND CONCLUSIONS

The model of thermodynamic consolidation of sea ice ridges is elaborated on the base of the laws of internal energy balance and salt diffusion in sea water. Self-similar problem

about the consolidation of homogeneous rubble ice filled half-space with initial porosity 0.3-0.4 is investigated. It is shown that the CL thickness is larger the level ice thickness in 1.5-2 times depending on the surface temperature. Numerical simulations of the consolidation of more realistic floating ridge show that the depth of consolidated ice depends on initial temperature of ice blocks composing the ridge and the distance between ice blocks. In considered example the bottom of consolidated ice reaches 7 m in the middle part of the ridge, and low temperature anomalies ~ -5^{o}C are conserved up to the depth 13 m inside the ridge. There is initial period of the consolidation about one week when atmosphere-ocean heat fluxes through the ridged ice are larger heat fluxes through the level ice with 1m thickness.

ACKNOWLDGMENTS

We are grateful to the Arctic and Antarctic Research Institute (St.-Petersburg, Russia), International Arctic Research Center and the Russian Foundation for Basic Research (Project Code 03-05-64833) for the support in the preparation of this paper.

REFERENCES

Hoyland, K. Simulations of the consolidation process in first-year sea ice ridges. *Cold Regions Scince and Technology* 34: 143-158 (2002).

Makshtas, A. The heat budget of Arctic ice in the winter. *International Glaciological Society*, Cambridge, (1991) 77 p.

Marchenko, A. The influence of ice ridge consolidation on atmosphere-ocean heat fluxes, In *Proceedings of the Arctic and Antarctic Research Institute* 446, G. Alekseev ed. Gidrometeoizdat, St.-Petersbugr, 150-164 (2003a). (in Russian)

Marchenko, A., Kim, H., Gudoshnokov, Yu., Zubakin, G., and Makshtas, A. Buildup and consolidation of sea ice ridges. In *Proceedings of the International Workshop on Frontier Technology in Ship and Ocean Engineering*, Seoul National University, Seoul 131-139 (2003b)**.**